



HAL
open science

Monte-Carlo estimation of geometric sensitivities in Solar Power Tower systems of flat mirrors

Zili HE, Paule Lapeyre, Stéphane Blanco, Simon Eibner, Mouna El-Hafi,
Richard Fournier

► **To cite this version:**

Zili HE, Paule Lapeyre, Stéphane Blanco, Simon Eibner, Mouna El-Hafi, et al.. Monte-Carlo estimation of geometric sensitivities in Solar Power Tower systems of flat mirrors. *Solar Energy*, 2023, 253, pp.9-29. 10.1016/j.solener.2023.02.013 . hal-03997190

HAL Id: hal-03997190

<https://imt-mines-albi.hal.science/hal-03997190>

Submitted on 21 Feb 2023

HAL is a multi-disciplinary open access archive for the deposit and dissemination of scientific research documents, whether they are published or not. The documents may come from teaching and research institutions in France or abroad, or from public or private research centers.

L'archive ouverte pluridisciplinaire **HAL**, est destinée au dépôt et à la diffusion de documents scientifiques de niveau recherche, publiés ou non, émanant des établissements d'enseignement et de recherche français ou étrangers, des laboratoires publics ou privés.

Monte-Carlo estimation of geometric sensitivities in Solar Power Tower systems of flat mirrors

Zili He^{1,*}, Paule Lapeyre², Stéphane Blanco³, Simon Eibner¹,
Mouna El Hafi¹, and Richard Fournier³

¹IMT Mines Albi, RAPSODEE - UMR CNRS 5302, Campus
Jarlard, 81013 Albi, France

²Department of Mechanical and Mechatronics Engineering,
University of Waterloo, 200 University Avenue West, Waterloo, ON
N2I 3G1, Canada

³LAPLACE - UMR CNRS 5213, 118, Route de Narbonne, 31062
Toulouse, France

*Corresponding author: zili.he@mines-albi.fr

February 20, 2023

Abstract

Optical optimizations for a Concentrated Solar Power (CSP) system are currently limited largely to gradient-free methods, since the gradient is hard to obtain by using the existing numerical optics tools available in the community. This article aims to build new algorithms of the Monte-Carlo type, which numerically estimate the gradient of power impacting the receiver with respect to the geometric parameters that characterize the geometric status of the heliostats in the heliostats field, for a Solar Power Tower (SPT) system.

Physical models will be built for the specific intensity and also for its derivatives to the geometric parameters of the heliostats, also called geometric sensitivities of intensity. Similar to the intensity but with their own models, they are regarded as physical quantities emitted, absorbed and reflected in the system. They carry the perturbations of intensity as information, corresponding to the relations between the geometric parameters and the physical events in the SPT system: blocking, spillage, shadowing, etc. These relations will be distinguished and discussed.

Finally, not only the gradient but also the contributions of physical events (blocking, spillage, shadowing, etc.) to the gradient can be estimated for further sensitivity analysis and optimization processes.

Nomenclature

| | | | |
|-------------------------|--|----------------------|--|
| I | Intensity | $\vec{a}_{i,\phi}$ | Axis of a heliostat for azimuth angle |
| N | Number of realizations of Monte-Carlo estimation | $\vec{a}_{i,\theta}$ | Axis of a heliostat for elevation angle |
| P | Total power impacting receiver | \vec{n}_i | Normal of a heliostat, $\vec{n}_i \in \mathcal{S}$ |
| $S_{i,j}$ | Sensitivity of Power | \vec{n}_r | Normal of the receiver, $\vec{n}_r \in \mathcal{S}$ |
| \mathbf{S} | Matrix of sensitivity of power | \vec{v} | Velocity of deformation |
| $\vec{\pi}$ | Matrix of parameters | \vec{x} | Position in the system, $\vec{x} \in \mathcal{G}$ |
| $\vec{\pi}_{i,j}$ | Geometric parameter of a heliostat | \vec{x}_b | Position on rearward surface of a heliostat, $\vec{x}_b \in \mathcal{H}_i^-$ |
| \mathcal{G} | Total set of the position in the system | \vec{x}_p | Position on reflecting surface of a heliostat, $\vec{x}_p \in \mathcal{H}_i^+$ |
| \mathcal{S} | Unit Sphere | \vec{x}_r | Position on receiver, $\vec{x}_r \in \mathcal{R}$ |
| \mathring{I} | Source of intensity | $n_{\vec{\pi}}$ | Number of parameters for each heliostat |
| \mathring{s} | Source of sensitivity | $n_{\mathcal{H}}$ | Number of heliostats |
| \mathring{s}^{blo} | Source of sensitivity: backward blocking | $s_{i,j}$ | Sensitivity of Intensity |
| \mathring{s}^{shad-b} | Source of sensitivity: backward shadowing | Acronyms | |
| \mathring{s}^{shad-f} | Source of sensitivity: forward shadowing | CBMC | Collision-Based Monte-Carlo algorithms |
| \mathring{s}^{tar} | Source of sensitivity: targeting | CSP | Concentrated Solar Power |
| \mathcal{H} | Heliostats, $\mathcal{H} \subset \partial\mathcal{G}$ | DNI | Direct Normal Irradiation |
| \mathcal{H}_i | A Heliostat, $\mathcal{H}_i \subset \mathcal{H}$ | IFMC | Integral Formulation Monte-Carlo |
| \mathcal{H}_i^+ | Reflecting surface of a heliostat, $\mathcal{H}_i^+ \subset \mathcal{H}_i$ | RTE | Radiative Transfer Equation |
| \mathcal{H}_i^- | Rearward surface of a heliostat, $\mathcal{H}_i^- \subset \mathcal{H}_i$ | SPT | Solar Power Tower |
| \mathcal{O}_l | Lower outline, $\mathcal{O}_l \subset \partial\mathcal{G}$ | Greek symbols | |
| \mathcal{O}_s | Upper outline, $\mathcal{O}_s \subset \partial\mathcal{G}$ | ρ | Reflectivity |
| \mathcal{R} | Receiver, $\mathcal{R} \subset \partial\mathcal{G}$ | σ | Standard deviation |
| $\partial\mathcal{G}$ | Total set of the position on the boundaries, $\partial\mathcal{G} \subset \mathcal{G}$ | Subscripts | |
| $\vec{\omega}$ | Direction in the system, $\vec{\omega} \in \mathcal{S}$ | b | Rearward surface of a heliostat |
| $\vec{\omega}_b$ | Direction attached on \vec{x}_b , $\vec{\omega}_b \in \mathcal{S}$ | i | Index of heliostat |
| $\vec{\omega}_c$ | Solar position: pointing from the center of the sun to \vec{x}_p . | j | Index of parameter of a heliostat |
| $\vec{\omega}_p$ | Direction attached on \vec{x}_p , $\vec{\omega}_p \in \mathcal{S}$ | k | Index of borders of a heliostat |
| $\vec{\omega}_r$ | Direction attached on \vec{x}_r , $\vec{\omega}_r \in \mathcal{S}$ | l | Lower outline |
| | | p | Reflecting surface of a heliostat |
| | | r | Receiver |
| | | s | Upper outline |

1 Introduction

Concentrating solar power (CSP) technology is one of the promising options to replace fossil fuel resources. Solar Power Tower (SPT) is a mature technology, and commercial facilities that follow this principle are currently in operation [1]. The optical system described by the heliostats field usually contributes to about 40% of the total cost of an SPT system[2]. The optical study of SPT systems has been an active research field [3–5]. Evaluations and optimizations of optical performance for SPT systems are essential.

As regards the evaluation of optical performance, there are two common categories of optical modeling methods: Monte-Carlo ray-tracing methods [6–9] and the cone optics convolution-based methods [10–12]. Compared to the latter kinds of method, the Monte-Carlo ray tracing methods are more versatile and can reproduce the real intersections of photons in complex geometries[13]. Several Monte-Carlo-based tools are compared to the convolution methods in the study[14], revealing that the Monte-Carlo methods have better performance in accuracy.

However, the optimizations of optical performance, which are usually related to geometric optimizations are limited largely to gradient-free methods [15, 16]. An important reason for choosing gradient-free methods is usually that ‘no gradient information is available from Monte-Carlo ray tracing methods’ [17, 18]. The gradient-based methods are usually used when the dimension of the parameter space of optimization is large [19], which is often the case in CSP optimization. Limited by the dimension of the parameter space, researchers can only perform optimization with small numbers of parameters. Diago *et al.* optimized only the height and the diameter of the tertiary concentrator in a Beam-Down system. In order to decrease the number of parameters to be optimized, Yu *et al.* optimized the aiming strategy by regrouping the heliostats, which point to some fixed points on the receiver. Furthermore, the gradient-free methods are usually treated as a “black box” tool, and the knowledge of the gradient helps to understand the parameters’ influences on the optimization’s objective.

Only a few studies have applied gradient-based methods to optimize the geometry of solar concentrators. Yang *et al.* [20] suggested approximating it by using area ratios. However, this method introduces an empiric weight. In studies carried out by Marston *et al.*, the gradient is approximated by a finite difference [21, 22], which is also called the resimulation method by Gobet [23]. However, beyond the fact that these studies deal only with simple geometrical situations, these authors claim that associated uncertainties are difficult to control. Regarding complex geometries such as a heliostat field in an SPT system with a large number of parameters, they cannot be treated in such a way (using finite difference approximation) because of the huge computational time and the lack of accuracy. Besides this approach of approximation, in the framework of Integral Formulation Monte-Carlo (IFMC) [24], the impacting power on the receiver in an SPT system is written as an integral formulation based on the physics of radiation. By differentiating and reformulating the corresponding integral formulation (for example, with respect to the angular spreading coefficient [24]), the gradient is also formulated as an integral formulation and can be estimated through

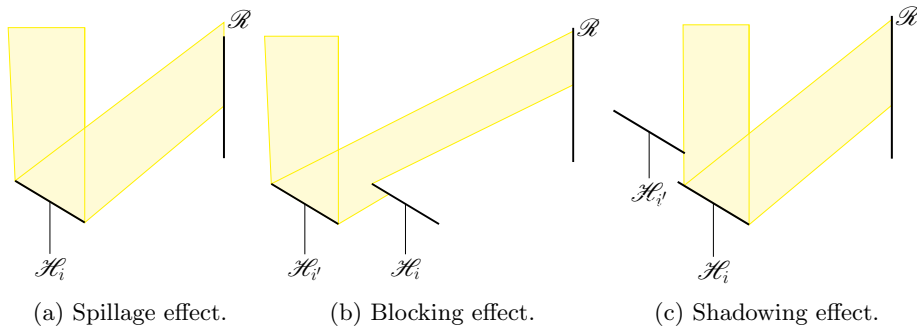


Figure 1: Spillage, blocking, and shadowing effects are common physical events in the SPT system. In this work, we further classify them into spillage, forward-blocking, backward-blocking, forward-shadowing, and backward-shadowing effects to estimate and analyze the sensitivity of geometric parameters. In the figure, \mathcal{H}_i and \mathcal{H}_j are the heliostats and \mathcal{R} is the receiver.

the Monte-Carlo method[25]. However, when the differentiated parameter is a geometric parameter that interacts in the integral domain (for example, the size of heliostats), great formal development efforts are needed[26]. Integrating this approach to a complex system such as the heliostats field of an SPT system seems nowadays to be impracticable. A very recent work [27] proposes an alternative to the work performed by [26]. This new approach proposes that the intensity and the geometric sensitivity of intensity (the derivative of the intensity with respect to a geometric parameter) should be regarded as two physical quantities emitted, transported, and intersected in a radiative system [27]. Based on this point of view, we can benefit from years of research in the radiative transfer field, on modeling the intensity to model the geometric sensitivity in an SPT system, making estimating the gradient in such a complex system possible. In parallel to our works, the literature shows that shape sensitivity calculations using the radiative transfer equation and its derivative has been the subject of much work in the computer graphics community [28–31]. Their objective is to reconstitute shapes to create the desired image by inversion. For many applications, such as remote sensing or deep neural networks for artificial intelligence [32] this “differentiable rendering” will become increasingly important in the coming years in this community. While we can take advantage of computer graphics tools to deal with the complex geometry of an SPT system, we still need to understand how the phenomena in SPT systems (blocking in Fig.1b, shadowing in Fig.1c, and spillage in Fig.1a) influence the sensitivities, which is also the objective of this work. Therefore, we will build a model of sensitivity and analyze the sources of the sensitivities in this model, which is specific to our approach [27, 33]. The sensitivities are propagated instead of the intensities following the Radiative Transport Equation (RTE) and the sensitivity sources are identified by this approach on the borders or on the surfaces of the studied system when we change geometric parameters. Consequently, we will see in this work that sensitivities can be presented in an intuitive manner: displacements and rotations of heliostats create sensitivity sources on the edges and surfaces of the heliostats that move according to different parameters of displacement and rotation.

As stated above, this paper aims to develop a method to estimate the

| unit | W/m |
|-------------------|-------------------|
| $S_{676,1}^{tar}$ | 70.63 ± 0.94 |
| $S_{676,1}^{blo}$ | -30.69 ± 0.58 |
| $S_{676,1}$ | 39.93 ± 1.51 |

Table 1: Sensitivity and its contributions (estimated values and their standard deviations) for the translation X of the 676th heliostat. For the 676th heliostat in Fig.2 (indexed as 676 in the table), the sensitivity of its translation X (indexed as 1 in the table) has two contributions. The translation will block its neighboring heliostat in its back ($S_{676,1}^{blo}$ is negative). However, the translation helps it to be blocked less by its neighboring heliostat on its front ($S_{676,1}^{tar}$ is positive). The sensitivity of translation X for this heliostat is then the sum of these two contributions ($S_{676,1}$).

geometric gradient (sensitivities) of SPT systems and to indicate how the blocking, spillage, and shadowing effects contribute to the gradient (sensitivities). The implementation of this method leads to different results that will be of interest to the SPT community to design (Fig.2a,2b,2c,2d) solar power plants, and also for their remote control (Fig.2e,2f). In Fig.2, x-y represents the ground plane, z is the height of the heliostat position, and each point is dedicated to a heliostat in the field. Furthermore, for each parameter of each heliostat, a detailed analysis of the contributions (spillage, blocking, shadowing) of sensitivity can be carried out (Table.1).

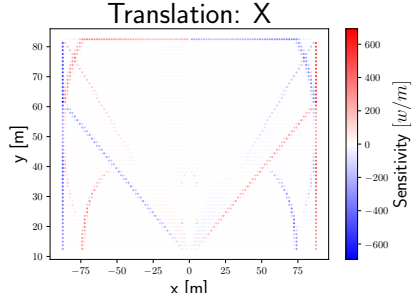
Finally, the article is organized into three parts:

- Section.2 provides the models of transport for the intensity and its derivative towards each heliostat five degrees of freedom (three translations and two rotations) and its size.
- Section.3 provides the integral formulations and algorithms to estimate the power collected by the receiver and the different sensitivities towards these six geometric parameters for each heliostat.
- Section.4 is dedicated to validation purposes: the estimation of the different sensitivities is compared to the approximation by the finite difference method. Comparisons and discussions about these two methods will be undertaken.

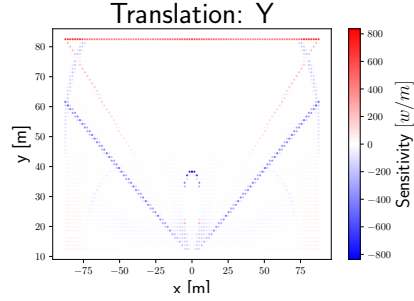
2 General models

In this work, we address the question of estimating the power P impacting the receiver of an SPT system with flat squared heliostats (Fig.3), as well as its derivatives $S_{i,j} \equiv \partial_{\tilde{\pi}_{i,j}} P$ of geometric parameters $\tilde{\pi}$ with i the index of a heliostat in the heliostats field and j the index of a geometric parameter ($j \in \{1, 2, 3, 4, 5, 6\}$, see Fig.4).

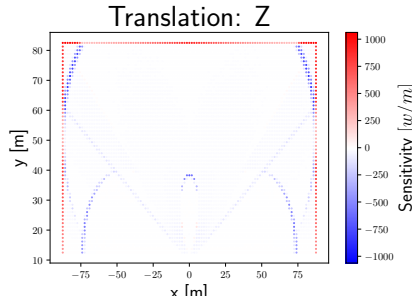
In order to numerically estimate P , we will build a model following the standard radiative transfer physics, using the intensity I as the descriptor. The transport of I in the medium is governed by a partial differential equation at any



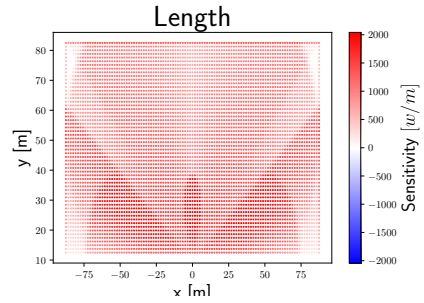
(a) Sensitivity of position-x for each heliostat.



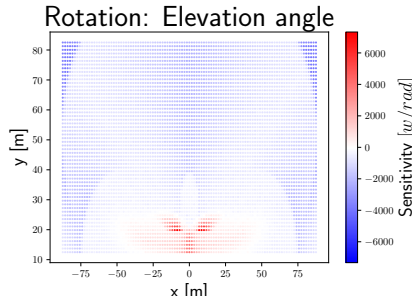
(b) Sensitivity of position-y for each heliostat.



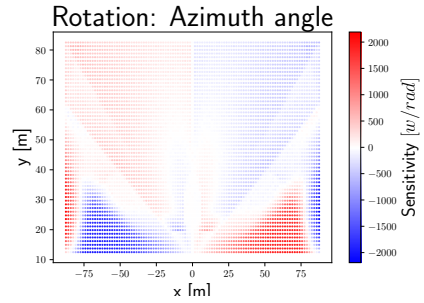
(c) Sensitivity of position-z for each heliostat.



(d) Sensitivity of the length of borders for each heliostat.



(e) Sensitivity of elevation angle for each heliostat.



(f) Sensitivity of azimuth angle for each heliostat.

Figure 2: Sensitivity of the total impacting power $P [w]$ for each heliostat in the field. Each point is dedicated to a heliostat, pointing to the center of the receiver at the moment of solar noon at the summer solstice. The layout corresponds to a real heliostat field: Sierra SunTower [34] (receiver at 50 m height at (0,0) and more details of the heliostats field are in Table.6 and Section.4.2). The corresponding color indicates its sensitivity with respect to its positions, rotations, and lengths. (10^6 Monte-Carlo realizations on each border of each heliostat and 10^8 Monte-Carlo realizations on each surface of heliostats).

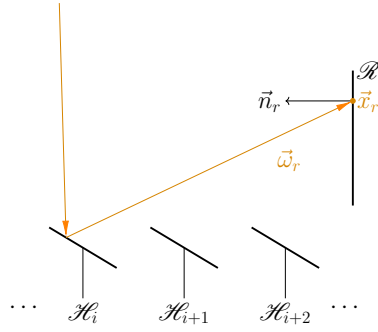


Figure 3: An SPT system consists of heliostats \mathcal{H}_i (with an index of i) on the ground and a receiver \mathcal{R} at the top of a tower.

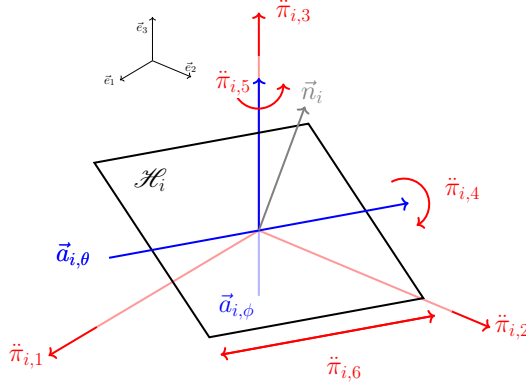


Figure 4: A heliostat (\mathcal{H}_i) has 5 degrees of freedom, which includes the translation ($\pi_{i,1}, \pi_{i,2}$ and $\pi_{i,3}$), following the three axes in the global coordinate system (\vec{e}_1, \vec{e}_2 and \vec{e}_3) and the rotation ($\pi_{i,4}$ and $\pi_{i,5}$) corresponding to an altazimuth mount according to the two vectors of rotation ($\vec{a}_{i,\theta}$ and $\vec{a}_{i,\phi}$). Also, the length of the size of the heliostat is included in this study ($\pi_{i,6}$). Those six parameters are indexed by j .

locations \vec{x} inside the field \mathcal{G} , following a vector of direction $\vec{\omega}$ in a unit sphere \mathcal{S} (RTE). On the boundaries $\partial\mathcal{G}$, the transport of I is governed by the boundary conditions, where the locations are noted with index, see Section.2.4 for details.

Equivalent to P , in order to numerically estimate $S_{i,j}$, we will build a radiative model in the medium and on the boundaries using the geometric sensitivity of intensity $s \equiv \partial_{\pi_{i,j}} I$ as the descriptor[27]. This descriptor carries the perturbation of I as information, corresponding to the relations between the geometric parameters $\pi_{i,j}$ and the physical events in the SPT system: blocking, spillage, shadowing, etc.

I and $s_{i,j}$ will be modeled locally in the medium and boundary conditions. After that, P and $S_{i,j}$ can be observed by formulating integral formulations of I and of $s_{i,j}$.

2.1 Definitions

2.1.1 Geometric sensitivity of intensity

The specific intensity used to model the STP system is considered independent of the wavelength [14, 35]. It is defined as $I \equiv I(\vec{x}, \vec{\omega}, \vec{\pi})$, where $\vec{\pi}$ is the matrix composed of $\pi_{i,j}$ (see Fig.4):

$$\vec{\pi} \equiv [\pi_{i,j}]. \quad (1)$$

\vec{x} , $\vec{\omega}$ and $\vec{\pi}$ are independent variables and matrix \mathbf{s} is defined as the derivative of I with respect to $\vec{\pi}$ [33]:

$$\mathbf{s}(\vec{x}, \vec{\omega}, \vec{\pi}) \equiv [s_{i,j}(\vec{x}, \vec{\omega}, \vec{\pi})] = \partial_{\vec{\pi}} I(\vec{x}, \vec{\omega}, \vec{\pi}). \quad (2)$$

The components of \mathbf{s} are:

$$s_{i,j}(\vec{x}, \vec{\omega}, \vec{\pi}) = \partial_{\pi_{i,j}} I(\vec{x}, \vec{\omega}, \vec{\pi}). \quad (3)$$

2.1.2 Geometric sensitivity of power

We implement this work within the framework of IFMC [24]. P can be estimated by the product of spatial integral and angular integral of incoming I on the receiver:

$$P(\vec{\pi}) = \int_{\mathcal{R}} d\vec{x}_r \int_{2\pi} |\vec{\omega}_r \cdot \vec{n}_r| d\vec{\omega}_r I(\vec{x}_r, \vec{\omega}_r, \vec{\pi}) \quad (4)$$

where \vec{x}_r is a position on the receiver, $\vec{\omega}_r$ the direction of observation, \vec{n}_r the normal of the receiver, and \mathcal{R} the absorbing surface of the receiver (see Fig.3).

Matrix \mathbf{S} is defined as the derivative of P with respect to $\vec{\pi}$, which can be developed in a straight forward way since \vec{x}_r and $\vec{\omega}_r$ are independent of $\vec{\pi}$ that characterizes only the heliostats:

$$\mathbf{S}(\vec{\pi}) \equiv [S_{i,j}(\vec{\pi})] = \int_{\mathcal{R}} d\vec{x}_r \int_{2\pi} |\vec{\omega}_r \cdot \vec{n}_r| d\vec{\omega}_r \mathbf{s}(\vec{x}_r, \vec{\omega}_r, \vec{\pi}). \quad (5)$$

The components of \mathbf{S} are:

$$S_{i,j}(\vec{\pi}) = \int_{\mathcal{R}} d\vec{x}_r \int_{2\pi} |\vec{\omega}_r \cdot \vec{n}_r| d\vec{\omega}_r s_{i,j}(\vec{x}_r, \vec{\omega}_r, \vec{\pi}). \quad (6)$$

We aim to estimate $P(\vec{\pi})$ and $S_{i,j}(\vec{\pi})$ by building a model of I and a model of $s_{i,j}$ in an SPT system.

2.2 Assumptions

The following assumptions are made for modeling I and $s_{i,j}$ in an SPT system:

1. The Pill-Box model is used to describe the sun shape (Eq.15).
2. The heliostats are considered perfectly specular, and beam pointing error is neglected.
3. The reflectivity of heliostats is considered homogeneous on the surface.
4. The medium between heliostats and the receiver is considered transparent.

It is noted that even though they are typical assumptions for modeling an SPT system, more realistic modelings can be realized based on the theoretical studies[27, 33] without specific difficulties (more realistic sun shape model, spatially and angularly inhomogeneous reflectivity, imperfect reflection, semi-transparent medium, etc.). In this work, we aim to build a basic model for I and $s_{i,j}$ in an SPT system. More realistic assumptions can be taken into account based on the developed basic model in this work. For example, if an angularly inhomogeneous reflectivity is considered in future work, it will have extra influences on the sensitivity with respect to the rotations of the heliostats. These extra influences can be considered as an additional source of sensitivity based on the developed model in this work.

2.3 Transport in the medium

2.3.1 Transport of intensity

The transport of intensity in the medium is modeled by RTE [36]. In an inhomogeneous medium, the collisions of absorption and scattering are described by the collision operator \mathcal{C} [29]:

$$\frac{\partial I(\vec{x}, \vec{\omega}, \vec{\pi})}{\partial \vec{x}} = \mathcal{C}[I(\vec{x}, \vec{\omega}, \vec{\pi})] + \kappa_a(\vec{x})I_b(\vec{x}) \quad (7)$$

with

$$\begin{aligned} \mathcal{C}[I(\vec{x}, \vec{\omega}, \vec{\pi})] = & \\ & - \kappa_a(\vec{x})I(\vec{x}, \vec{\omega}, \vec{\pi}) \\ & - \kappa_s(\vec{x})I(\vec{x}, \vec{\omega}, \vec{\pi}) \\ & + \frac{1}{4\pi} \int_{\omega'=4\pi} \kappa_s(\vec{x})I(\vec{x}, \vec{\omega}', \vec{\pi})\Phi(\vec{\omega}', \vec{\omega})d\vec{\omega}' \end{aligned} \quad (8)$$

where κ_a is the absorption coefficient, κ_s the scattering coefficient, \vec{x} the position vector in the medium, $\vec{\omega}$ the vector of propagation and $\Phi(\vec{\omega}', \vec{\omega})$ is the phase-function. Under the assumption of local thermal equilibrium, the source $\kappa_a(\vec{x})I_b(\vec{x})$ (in Eq.7) is isotropic and is a function of temperature, and I_b is the specific intensity at equilibrium following the Planck's law.

In this work, we will consider a transparent and cold medium (where $\kappa_s = 0$, $\kappa_a = 0$, and $I_b(\vec{x}) = 0$). Therefore, the equation of transport for I used in this work is:

$$\frac{\partial I(\vec{x}, \vec{\omega}, \vec{\pi})}{\partial \vec{x}} = 0 \quad (9)$$

2.3.2 Transport of geometric sensitivity of intensity

We differentiate Eq.7 with respect to the geometric parameter $\vec{\pi}$ on the both sides:

$$\frac{\partial^2 I(\vec{x}, \vec{\omega}, \vec{\pi})}{\partial \vec{x} \partial \vec{\pi}} = \frac{\partial [\mathcal{C}[I(\vec{x}, \vec{\omega}, \vec{\pi})]]}{\partial \vec{\pi}} \quad (10)$$

Referring to the definition of the sensitivity (Eq.2), the following equation transport is yielded:

$$\frac{\partial \mathbf{s}(\vec{x}, \vec{\omega}, \vec{\pi})}{\partial \vec{x}} = \mathcal{C}[\mathbf{s}(\vec{x}, \vec{\omega}, \vec{\pi})] \quad (11)$$

The development from Eq.7 to Eq.11 is relatively straightforward. First, it is because the medium's properties (κ_a, κ_s, Φ and I_b) are not dependent on $\vec{\pi}$, and secondly, $\vec{x}, \vec{\omega}$ and $\vec{\pi}$ are three independent variables.

Referring to Eq.2 and Eq.3, the equation of transport of each of the component $s_{i,j}$ is [33]:

$$\frac{\partial s_{i,j}(\vec{x}, \vec{\omega}, \vec{\pi})}{\partial \vec{x}} = \mathcal{C}[s_{i,j}(\vec{x}, \vec{\omega}, \vec{\pi})] \quad (12)$$

with \mathcal{C} the same collision operator as it is in Eq.8:

$$\begin{aligned} \mathcal{C}[s_{i,j}(\vec{x}, \vec{\omega}, \vec{\pi})] = & \\ & - \kappa_a(\vec{x}) s_{i,j}(\vec{x}, \vec{\omega}, \vec{\pi}) \\ & - \kappa_s(\vec{x}) s_{i,j}(\vec{x}, \vec{\omega}, \vec{\pi}) \\ & + \frac{1}{4\pi} \int_{\omega'=4\pi} \kappa_s(\vec{x}) s_{i,j}(\vec{x}, \vec{\omega}', \vec{\pi}) \Phi(\vec{\omega}', \vec{\omega}) d\vec{\omega}' \end{aligned} \quad (13)$$

Finally, the collision operator \mathcal{C} is also applied to the geometric sensitivities when describing its transport in the medium. $s_{i,j}$ can be regarded as a physical quantity transported in the medium. Similar to the intensity I , the sensitivity of intensity $s_{i,j}$ is also absorbed and scattered. This new point of view allows us to study the geometric sensitivity of intensity practically, benefiting from years of research in the transport of intensity in the physics of radiative transfer.

In this work, we will consider a transparent and cold medium. The intensity and the geometric sensitivity will have the same model of transport in the medium:

$$\frac{\partial s_{i,j}(\vec{x}, \vec{\omega}, \vec{\pi})}{\partial \vec{x}} = 0 \quad (14)$$

In order to create a similar physical picture for the transport of I and $s_{i,j}$ in the medium, we can consider that the medium is also 'transparent' for the geometric sensitivities $s_{i,j}$.

2.4 Boundary conditions

I and $s_{i,j}$ are transported following Eq.9 and Eq.14 in the medium, while on the boundaries, they can be emitted, reflected, or absorbed.

Seeing Fig.5, positions and directions on the boundaries are noted with an index of s on \mathcal{O}_s , r on \mathcal{R} , p on \mathcal{H}_i^+ , b on \mathcal{H}_i^- and O_l on \mathcal{O}_l . We will build the boundary conditions for I and then differentiate them with respect to $\vec{\pi}_{i,j}$ to establish the boundary conditions for $s_{i,j}$.

2.4.1 Upper outline \mathcal{O}_s

In an SPT system, the only source of intensity is the sun. Most of the time, we use the sun-shape models, which are usually angular functions, to describe the arriving intensity in the system[14, 37, 38]. To be noticed that this work is a stationary study, which means it is established for a fixed solar position.

The pill-box sun shape is used in this work:

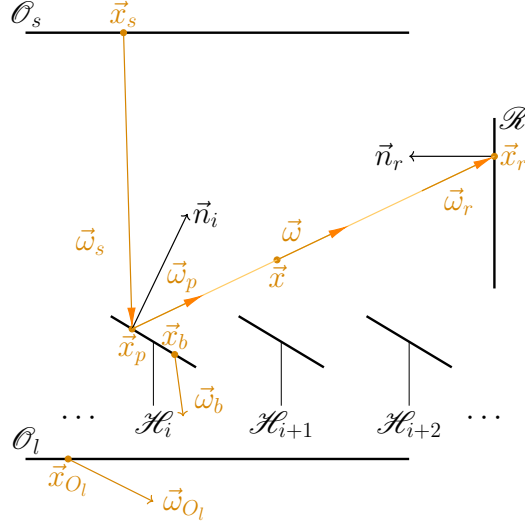


Figure 5: The system consists of heliostats \mathcal{H}_i (with index of i) on the ground with \mathcal{H}_i^+ its reflecting surface and \mathcal{H}_i^- its rearward surface, a receiver \mathcal{R} , an upper outline \mathcal{O}_s and a lower outline \mathcal{O}_l . Solar intensity is reflected by \mathcal{H}_i^+ and collected on the \mathcal{R} .

$$I(\vec{x}_s, \vec{\omega}_s, \vec{\pi}) \equiv \dot{I}(\vec{\omega}_s) = I_0 \mathcal{H}(\vec{\omega}_s \cdot \vec{\omega}_c - \cos(\theta_{disk})) \quad (15)$$

where $\vec{\omega}_c$ is a vector that characterizes the solar position (fixed in this work), I_0 the constant intensity coming from the sun, \mathcal{H} the Heaviside function and $\theta_{disk} = 0.0046 \text{ rad}$ the radial angular radius of the solar disk. Moreover, this boundary condition is noted \dot{I} because it is the source of I in the system.

The upper outline \mathcal{O}_s can be considered emitting intensity towards the system, but it is not reflecting the incoming intensity. Therefore, this boundary can be considered as a ‘black body’ for I .

The derivative of I on \mathcal{O}_s with respect to $\vec{\pi}_{i,j}$ is therefore null, because $\vec{\pi}_{i,j}$ characterizes the geometry of heliostats instead of \mathcal{O}_s :

$$s_{i,j}(\vec{x}_s, \vec{\omega}_s, \vec{\pi}) = 0. \quad (16)$$

Following Eq.16, no $s_{i,j}$ is emitted by the sun, and all $s_{i,j}$ transported to the upper outline \mathcal{O}_s are not reflected but absorbed. Therefore, in order to create a similar physical picture for the transport of I and $s_{i,j}$ on the boundaries, \mathcal{O}_s can be regarded as a ‘cold black body’ for $s_{i,j}$.

2.4.2 Receiver \mathcal{R} and lower outline \mathcal{O}_l

\mathcal{R} and \mathcal{O}_l in our system (Fig.5) are considered ‘cold black body’ for I . All the intensity is not hitting the heliostats, and the receiver will be lost. The radiative emission of the receiver is not included in the model since the heat transfer of the receiver is out of the scope of this work.

The boundary conditions of receiver \mathcal{R} and lower outline \mathcal{O}_l are then established:

$$\begin{cases} I(\vec{x}_r, -\vec{\omega}_r, \vec{\pi}) = 0 \\ I(\vec{x}_{O_l}, -\vec{\omega}_{O_l}, \vec{\pi}) = 0 \end{cases} \quad (17)$$

where $-\vec{\omega}_r$ and $-\vec{\omega}_{O_l}$ are the outgoing direction of propagation of I from the receiver and the lower outline (Fig.5).

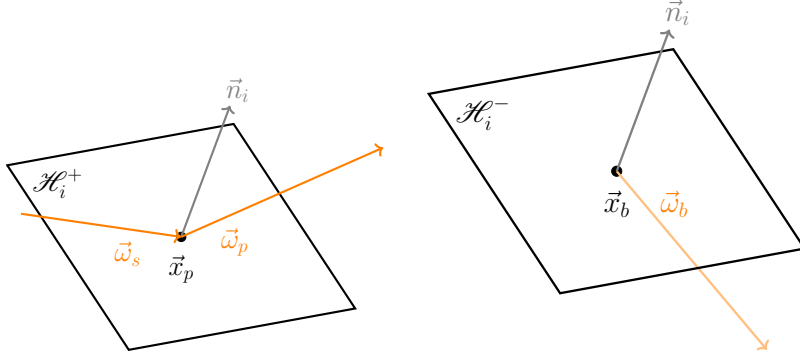
Since $\vec{\pi}_{i,j}$ only characterizes the heliostats, there are no $s_{i,j}$ going out from these boundaries:

$$\begin{cases} s_{i,j}(\vec{x}_r, -\vec{\omega}_r, \vec{\pi}) = 0 \\ s_{i,j}(\vec{x}_{O_l}, -\vec{\omega}_{O_l}, \vec{\pi}) = 0. \end{cases} \quad (18)$$

In order to create a similar physical picture for the transport of I and $s_{i,j}$ on the boundaries, \mathcal{R} and \mathcal{O}_l can also be regarded as ‘cold black body’ for $s_{i,j}$. All $s_{i,j}$ that are not hitting the heliostat or the receiver will be lost, and $s_{i,j}$ are not emitted from these boundaries.

2.4.3 Heliostat \mathcal{H}_i

Intensity: We define \vec{n}_i as the normal of the reflecting surface of \mathcal{H}_i . The boundary conditions of I on a heliostat \mathcal{H}_i are modeled separately by two parts: one for the reflecting surface \mathcal{H}_i^+ (where $\vec{\omega}_p \cdot \vec{n}_i > 0$), the other for the rearward surface \mathcal{H}_i^- (where $\vec{\omega}_b \cdot \vec{n}_i < 0$), see Fig.6. Also, the heliostats are considered ‘cold’, which means they do not emit intensity.



(a) Reflecting surface where $\vec{\omega}_p \cdot \vec{n}_i > 0$ (b) Rearward surface where $\vec{\omega}_b \cdot \vec{n}_i < 0$

Figure 6: Orientation convention of the heliostat \mathcal{H}_i

The transport of intensity on the reflecting surface of the heliostat can be described by:

$$I(\vec{x}_p, \vec{\omega}_p, \vec{\pi}) = \rho I(\vec{x}_p, \vec{\omega}_s, \vec{\pi}) \quad (19)$$

where ρ is the reflectivity, $I(\vec{x}_p, \vec{\omega}_s, \vec{\pi})$ the incoming intensity and $\vec{\omega}_p$ the direction reflected by heliostat of $\vec{\omega}_s$ (Fig.6a).

The transport of I on the rearward surface of \mathcal{H}_i can be described by:

$$I(\vec{x}_b, \vec{\omega}_b, \vec{\pi}) = 0. \quad (20)$$

The rearward surface of \mathcal{H}_i is also considered a ‘cold black body’.

Geometric sensitivity of intensity: The development of the boundary conditions of $s_{i,j}$ for \mathcal{H}_i is less straightforward. [33] proposed a model of geometric sensitivity on reflecting surfaces. Based on this model, the boundary conditions of $s_{i,j}$ is yielded for reflecting surface (Eq.21, referring to Fig.6a) and also for the rearward surface (Eq.22, referring to Fig.6b). It is found that the boundary condition of the reflecting surface contains emission terms (the sources) and a reflection term, see details in Appendix.A.

$$s_{i,j}(\vec{x}_p, \vec{\omega}_p, \vec{\pi}) = \hat{s}_{i,j}(\vec{x}_p, \vec{\omega}_p, \vec{\pi}) + \rho s_{i,j}(\vec{x}_p, \vec{\omega}_s, \vec{\pi}) \quad (21)$$

$$s_{i,j}(\vec{x}_b, \vec{\omega}_b, \vec{\pi}) = \hat{s}_{i,j}(\vec{x}_b, \vec{\omega}_b, \vec{\pi}) \quad (22)$$

We note $\hat{s}_{i,j}$ as the sources of $s_{i,j}$ (as we noted \hat{I} as the source of I).

The sources $\hat{s}_{i,j}$ can be physically regarded as the local perturbations of I with respect to $\vec{\pi}_{i,j}$ on \mathcal{H}_i , while $s_{i,j}$ is such perturbations transported in the radiative system (see Fig.7). Usually, the sources of sensitivity $\hat{s}_{i,j}$ are functions of I , where the two models of transport are coupled.

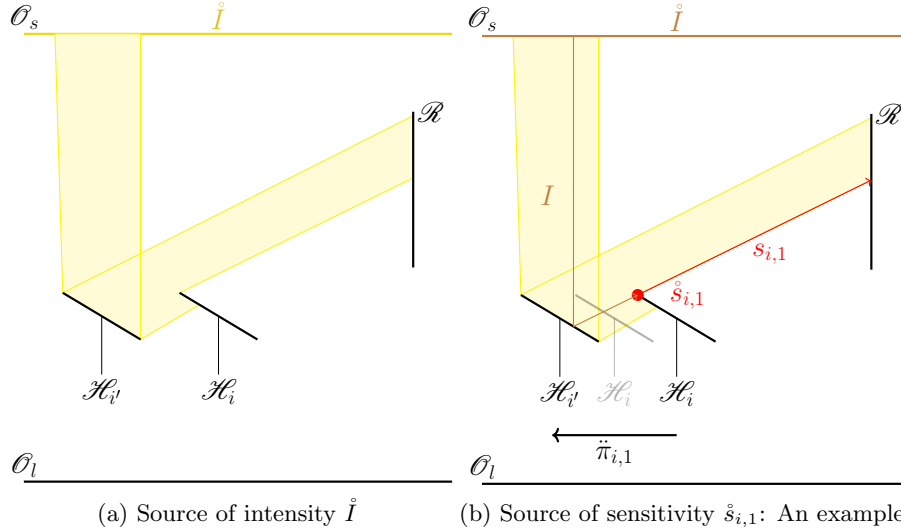


Figure 7: The source of intensity is on the boundary \mathcal{O}_s . In this example, The source of sensitivity is on the border of heliostat \mathcal{H}_i because the perturbation of $\vec{\pi}_{i,1}$ will create locally a perturbation of I on the border of \mathcal{H}_i , which causes a perturbation of P . Also, the source $\hat{s}_{i,j}$ is coupled with the arrived intensity \hat{I} . Therefore, the model of $s_{i,j}$ is coupled with the model of I . The optical path of $s_{i,j}$ is in red, and the coupled optical path of I is in brown.

Moreover, different types of perturbations (sources) are distinguished, related to blocking, shadowing, and spillage effects. Therefore, we further classify the sources by their contributions to these different physical effects.

For the reflecting surface \mathcal{H}_i^+ :

$$\hat{s}_{i,j}(\vec{x}_p, \vec{\omega}_p, \vec{\pi}) = \hat{s}_{i,j}^{tar}(\vec{x}_p, \vec{\omega}_p, \vec{\pi}) + \hat{s}_{i,j}^{blo}(\vec{x}_p, \vec{\omega}_p, \vec{\pi}) + \hat{s}_{i,j}^{shad-b}(\vec{x}_p, \vec{\omega}_p, \vec{\pi}) \quad (23)$$

and for the rearward surface \mathcal{H}_i^- :

$$\mathring{s}_{i,j}(\vec{x}_b, \vec{\omega}_b, \ddot{\mathbf{n}}) = \mathring{s}_{i,j}^{shad-f}(\vec{x}_b, \vec{\omega}_s, \ddot{\mathbf{n}}). \quad (24)$$

$\mathring{s}_{i,j}^{tar}$ is named the source of targeting. It is the perturbation caused by the targeting or missing of the reflected intensity on \mathcal{H}_i^+ , with respect to $\ddot{\pi}_{i,j}$. It is separated into two parts:

$$\mathring{s}_{i,j}^{tar} = \mathring{s}_{i,j}^{tar,spatial} + \mathring{s}_{i,j}^{tar,angular}. \quad (25)$$

$\mathring{s}_{i,j}^{tar,spatial}$ is originated from the change of position of \mathcal{H}_i with respect to $\ddot{\pi}_{i,j}$, located on the border of \mathcal{H}_i^+ (see Fig.8 for an example of $\ddot{\pi}_{i,1}$). $\mathring{s}_{i,j}^{tar,angular}$ is originated from the change of normal, located on the surface of \mathcal{H}_i^+ (see Fig.9 for an example of $\ddot{\pi}_{i,4}$, but to be noted that perturbation of $\ddot{\pi}_{i,4}$ leads to the change of position and also the change of normal).

Concerning the change of position, the sources $\mathring{s}_{i,j}^{tar,spatial}$ are located on the border of the heliostat (see formal developments in Appendix.A and Appendix.B). If we note the sum of $\mathring{s}_{i,j}^{tar,spatial}$ captured on \mathcal{R} to be $S_{i,j}^{tar,spatial}$, it will be 0 when $\mathring{s}_{i,j}^{tar,spatial}$ are all captured or all missed, see Fig.8. However, when the spillage effect (Fig.8c), forward-blocking effect (Fig.8d) or backward-shadowing effect (Fig.8e) occurs, the perturbation of $\ddot{\pi}_{i,j}$ will perturb these effects and $\mathring{s}_{i,j}^{tar,spatial}$ will be partially captured. Therefore, $S_{i,j}^{tar,spatial}$ will be non-null.

Concerning the change of normal, the sources $\mathring{s}_{i,j}^{tar,angular}$ are located on the surface of the heliostat (see details in Appendix.A and Appendix.B). If we note the sum of $\mathring{s}_{i,j}^{tar,angular}$ captured on \mathcal{R} to be $S_{i,j}^{tar,angular}$, it will be non-null when $\mathring{s}_{i,j}^{tar,angular}$ is all captured on \mathcal{R} since the perturbation of $\ddot{\pi}_{i,j}$ perturbs the cosine effect, and it will be 0 when all is missing, see Fig.9. Moreover, when the spillage effect (Fig.9c), forward-blocking effect (Fig.9d) or backward-shadowing effect (Fig.9e) occurs, the perturbation of $\ddot{\pi}_{i,j}$ will perturb these effects and $\mathring{s}_{i,j}^{tar,angular}$ will be partially captured.

We must distinguish the contributions from backward and forward shadowing in the model of $s_{i,j}$. Backward-shadowing means that the perturbation of $\ddot{\pi}_{i,j}$ affects the shadows on the heliostat itself Fig.10a. Forward-shadowing means that the perturbation of $\ddot{\pi}_{i,j}$ affects the shadows on a neighboring heliostat Fig.11.

$\mathring{s}_{i,j}^{shad-b}$ is named the source of backward-shadowing. This perturbation is observed on the surface of \mathcal{H}_i^+ , but originated from the border of a neighboring heliostat, see Fig.10a and 10b. It is also separated by two parts, corresponding to the change of position and direction of \mathcal{H}_i :

$$\mathring{s}_{i,j}^{shad-b} = \mathring{s}_{i,j}^{shad-b,spatial} + \mathring{s}_{i,j}^{shad-b,angular} \quad (26)$$

We note $S_{i,j}^{shad-b,spatial}$ as the sum of the source $\mathring{s}_{i,j}^{shad-b,spatial}$ captured on \mathcal{R} . When backward-shadowing occurs, the perturbation of $\ddot{\pi}_{i,j}$ will perturb the effect of backward-shadowing by the change of position (see an example of $\ddot{\pi}_{i,1}$ in Fig.10a) and $S_{i,j}^{shad-b,spatial} \neq 0$.

We note $S_{i,j}^{shad-b,angular}$ as the sum of the source $\mathring{s}_{i,j}^{shad-b,angular}$ captured on \mathcal{R} . When backward-shadowing occurs, the perturbation of $\ddot{\pi}_{i,j}$ will perturb

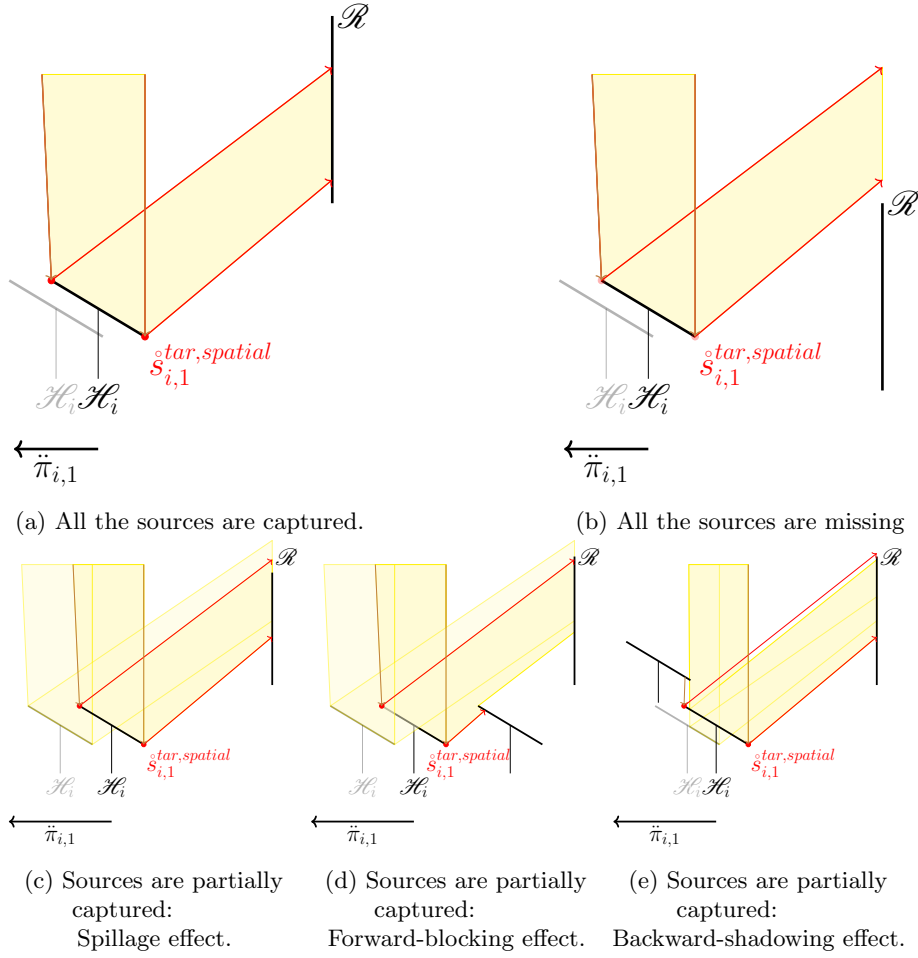


Figure 8: The optical path of I is in yellow, and that of $s_{i,j}$ is in red. When all the sources of $s_{i,1}^{tar,spatial}$ are all captured by \mathcal{R} or they are all missing, the perturbation of $\ddot{\pi}_{i,1}$ is not causing the perturbation of P and $S_{i,1}^{tar,spatial} = 0$. When spillage effect, forward-blocking effect, or backward-shadowing effect occurs, $s_{i,1}^{tar,spatial}$ is partially captured by \mathcal{R} and $S_{i,1}^{tar,spatial} \neq 0$.

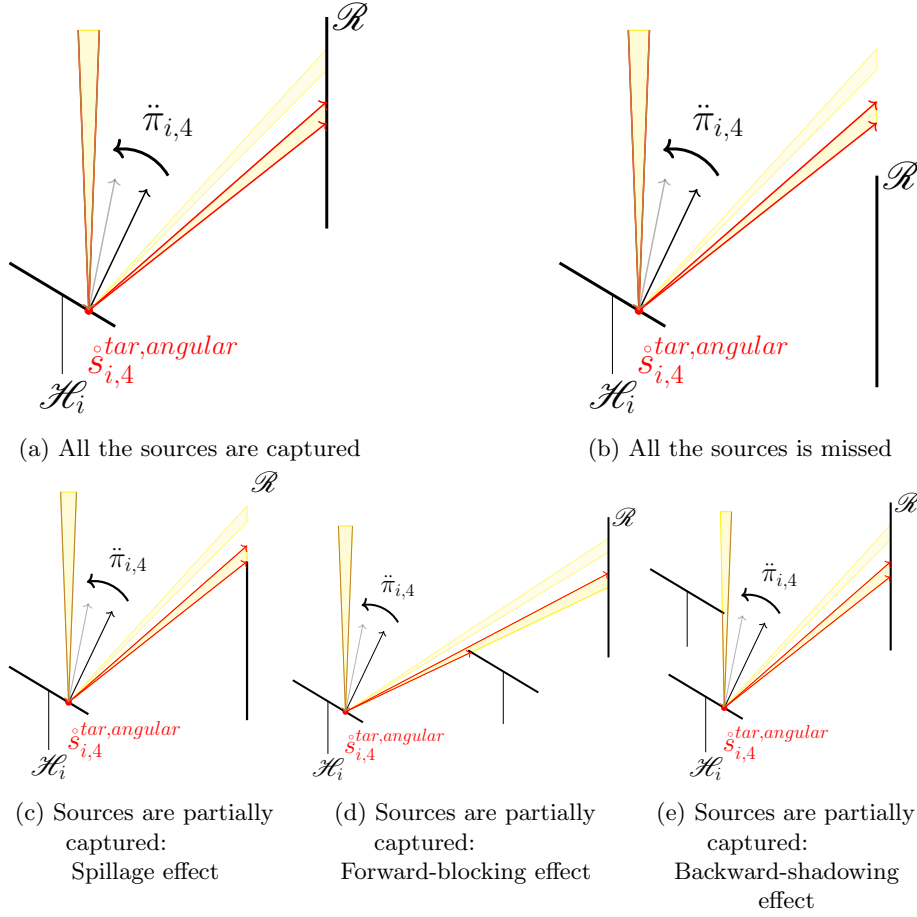


Figure 9: With a perturbation of $\ddot{\pi}_{i,4}$, the perturbation of I is observed on all surfaces of \mathcal{H}_i and borders of Ω_s (the solar cone). When all the sources of $\mathring{s}_{i,1}^{tar,angular}$ is all captured on $\mathcal{R}_{i,1}$, the perturbation of $\ddot{\pi}$ causes the perturbation of P because of the cosine effect and $S_{i,1}^{tar,angular} \neq 0$. When all the sources are missing, $S_{i,1}^{tar,angular} = 0$. Finally, when the spillage effect, forward-blocking effect or backward-shadowing effect occurs, $\mathring{s}_{i,1}^{tar,angular}$ is partially captured by \mathcal{R} and $S_{i,1}^{tar,angular} \neq 0$.

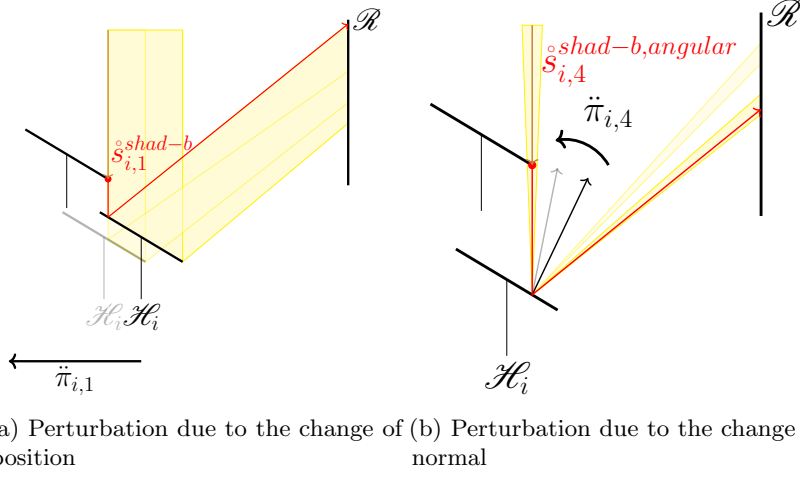


Figure 10: When the backward shadowing effect occurs, with a perturbation of $\tilde{\pi}_{i,4}$, P is perturbed because of its change of normal. The source of sensitivity $\dot{s}_{i,4}^{shad-b}$ is on the border of the neighboring heliostat. P is also perturbed because of its change of position. The source of sensitivity $\dot{s}_{i,1}^{shad-b}$ is on the border of the neighboring heliostat. The backward-shadowing is about the shadowing effect created by the neighboring heliostat.

the effect of backward-shadowing by the change of normal (see an example of $\tilde{\pi}_{i,4}$ in Fig.10b) and $S_{i,j}^{shad-b,spatial} \neq 0$.

$\dot{s}_{i,j}^{shad-f}$ is named the source of forward-shadowing. This perturbation of I is caused by the creation of shadows. With a perturbation of $\tilde{\pi}_{i,j}$, shadows might be created on another heliostat in the field.

We note $S_{i,j}^{shad-f}$ as the sum of the source $\dot{s}_{i,j}^{shad-f}$ captured on \mathcal{R} . When forward-shadowing occurs, a perturbation of $\tilde{\pi}_{i,j}$ will perturb the effect of forward-shadowing (see an example of $\tilde{\pi}_{i,1}$ in Fig.11) and $S_{i,j}^{shad-f} \neq 0$.

$\dot{s}_{i,j}^{blo}$ is named the source of backward-blocking. This perturbation of I is caused by blocking. With a perturbation of $\tilde{\pi}_{i,j}$, \mathcal{H}_i might block the I reflected on another heliostat in the field.

We note $S_{i,j}^{blo}$ as the sum of the source $\dot{s}_{i,j}^{blo}$ captured on \mathcal{R} . When backward-blocking occurs, a perturbation of $\tilde{\pi}_{i,j}$ will perturb the effect of backward-blocking (see an example of $\tilde{\pi}_{i,1}$ in Fig.12) and $S_{i,j}^{blo} \neq 0$. Finally, the geometric sensitivity of power $S_{i,j}$ is the sum of all captured sources:

$$S_{i,j} = S_{i,j}^{tar} + S_{i,j}^{blo} + S_{i,j}^{shad-b} + S_{i,j}^{shad-f} \quad (27)$$

with

$$S_{i,j}^{tar} = S_{i,j}^{tar,spatial} + S_{i,j}^{tar,angular} \quad (28)$$

and

$$S_{i,j}^{shad-b} = S_{i,j}^{shad-b,spatial} + S_{i,j}^{shad-b,angular}. \quad (29)$$

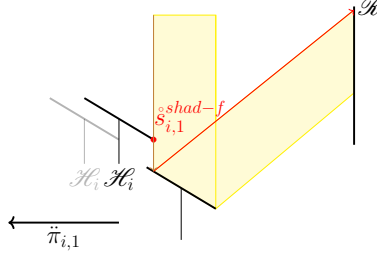


Figure 11: When the forward-shadowing effect occurs, with a perturbation of $\ddot{\pi}_{i,1}$, a perturbation of P is observed. The source of sensitivity $\dot{s}_{i,1}^{shad-f}$ is on the border of the heliostat itself. The forward-shadowing is about the shadowing effect created by the heliostat itself.

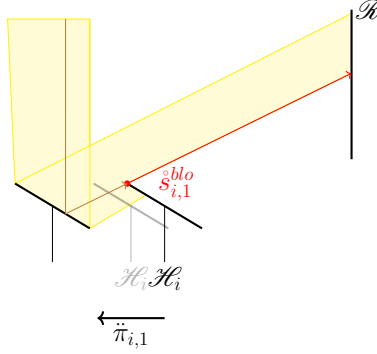


Figure 12: When the backward-blocking effect occurs, a perturbation of $\ddot{\pi}_{i,1}$ causes the perturbation of P . This is because $\ddot{\pi}$ characterizes how much intensity reflected is blocked by \mathcal{H}_i . The source of sensitivity $\dot{s}_{i,j}^{blo}$ is on the border of \mathcal{H}_i^+ .

Each contribution in Eq.27 is the sum of the sources $\dot{s}_{i,j}$ captured by the receiver respectively:

$$\begin{bmatrix} S_{i,j}^{star}(\ddot{\pi}) \\ S_{i,j}^{blo}(\ddot{\pi}) \\ S_{i,j}^{shad-b}(\ddot{\pi}) \\ S_{i,j}^{shad-f}(\ddot{\pi}) \end{bmatrix} = \int_{\mathcal{R}} d\vec{x}_r \int_{2\pi} |\vec{\omega}_r \cdot \vec{n}_r| d\vec{\omega}_r \begin{bmatrix} \dot{s}_{i,j}^{star}(\vec{x}_r, \vec{\omega}_r, \ddot{\pi}) \\ \dot{s}_{i,j}^{blo}(\vec{x}_r, \vec{\omega}_r, \ddot{\pi}) \\ \dot{s}_{i,j}^{shad-b}(\vec{x}_r, \vec{\omega}_r, \ddot{\pi}) \\ \dot{s}_{i,j}^{shad-f}(\vec{x}_r, \vec{\omega}_r, \ddot{\pi}) \end{bmatrix}. \quad (30)$$

3 Algorithms

In the previous section, general models for the intensity I and its derivatives $s_{i,j}$ are built for an SPT system. Based on the models, we aim to build algorithms

to estimate the impacting power P and the matrix \mathbf{S} by the Monte-Carlo ray tracing method.

Concerning the model of intensity I , the only source is the intensity from the sun \dot{I} located on the surface that delimits the sky, \mathcal{O}_s . P will be estimated by summing the source \dot{I} captured on the receiver \mathcal{R} (see Eq.4).

Concerning the model of $s_{i,j}$, there are several sources of sensitivities on the heliostat \mathcal{H}_i . $S_{i,j}$ will be estimated by summing all the sources $\dot{s}_{i,j}$ captured on the receiver \mathcal{R} (see Eq.5).

The corresponding statistical ray tracing process can start from the receiver looking for the sources or, inversely, from the sources located on the heliostat, looking for the receiver. The strategy of proceeding statistical ray tracing process has enormous influences on the convergence rate.

In order to estimate the impacting power P , unlike the Collision-Based Monte-Carlo algorithms (CBMC) where the ray-tracing starts from a plane above reflectors (\mathcal{O}_s in our case)[7], we integrate this work in the framework of IFMC, starting the ray-tracing process from the reflecting surfaces (\mathcal{H}^+ in our case), which improves convergence rate[14, 24].

In order to estimate the matrix of sensitivity \mathbf{S} , we start the statistical ray-tracing process by the sources, looking for the receiver \mathcal{R} .

3.1 Estimation of impacting power

The algorithm to compute the impacting power by IFMC has been thoroughly described by [24, 39]. Here is a quick reminder of the integral formulation for estimating P under the assumptions made in Section.2.2:

$$P = \int_{\mathcal{H}^+} p_X(\vec{x}_{p1}) d\vec{x}_{p1} \int_{\Omega_s} p_{\Omega_s}(\vec{\omega}_s) d\vec{\omega}_s \{ \mathcal{H}(\vec{x}_{p0} \in \mathcal{O}_s) \mathcal{H}(\vec{x}_{p2} \in \mathcal{R}) \hat{w} \} \quad (31)$$

with

$$p_X(\vec{x}_{p1}) = \frac{1}{\mathcal{S}_{\mathcal{H}^+}}, \quad (32)$$

$$p_{\Omega_s}(\vec{\omega}_s) = \frac{1}{\int_C d\vec{\omega}_s} = \frac{1}{2\pi(1 - \cos \theta_{disk})} \quad (33)$$

$$\hat{w} = DNI\rho|\vec{\omega}_s \cdot \vec{n}_i| \mathcal{S}_{\mathcal{H}^+} \quad (34)$$

where $\mathcal{S}_{\mathcal{H}^+}$ is the area of all reflected surfaces of the heliostats field.

Equation 31 is the integral formulation of the model to compute the impacting power P and can also be seen as an expected value which is the core of an IFMC algorithm. The expected value P can be estimated by the mean operator (Algo.2 in Appendix.E):

$$P \approx \frac{1}{N} \sum_{q=1}^N [\mathcal{H}(\vec{x}_{p0,q} \in \mathcal{O}_s) \mathcal{H}(\vec{x}_{p2,q} \in \mathcal{R}) \hat{w}_q] \quad (35)$$

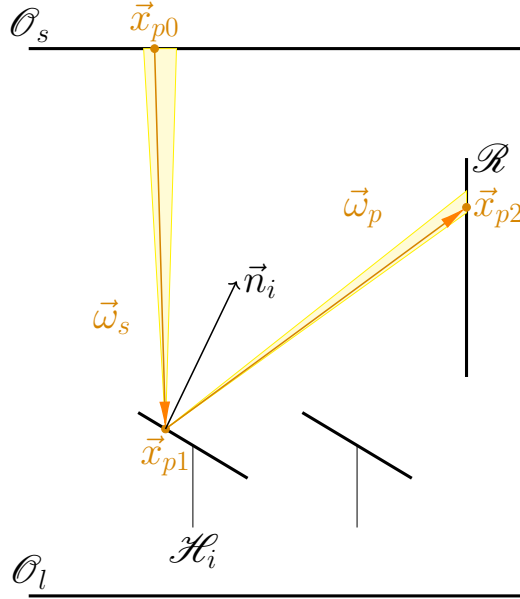


Figure 13: In order to estimate P , for each realization, the algorithm starts by uniformly sampling a random position \vec{x}_{p1} (following Eq.32) on the reflected surface of the whole heliostat field \mathcal{H}^+ . Then, a direction is sampled within the solar cone Ω_s of angular radius θ_{disk} following the density of probability p_{Ω_s} (Eq.33). In order to check if the shadowing effect occurs, \vec{x}_{p0} is defined as the first intersection with a boundary of the system, starting at \vec{x}_{p1} in the direction $-\vec{\omega}_s$, and it is tested if \vec{x}_{p0} belongs to \mathcal{O}_s . If there is no shadowing, the reflected direction $\vec{\omega}_p$ is computed based on the law of reflection for specular surfaces from the sampled $\vec{\omega}_s$ and the local normal \vec{n}_i at position \vec{x}_{p1} . In order to check if the spillage or the blocking effect occurs, \vec{x}_{p2} is defined as the first intersection with a boundary of the system, starting at \vec{x}_{p1} in the direction $\vec{\omega}_p$, and it is tested if \vec{x}_{p2} belongs to \mathcal{R} . Finally, if no shadowing nor blocking occurs, the weight of Monte-Carlo for this realization \hat{w} is computed.

where $\vec{x}_{p0,q}$ and $\vec{x}_{p2,q}$ are obtained through the described ray-tracing algorithm on Fig.13 for the q^{th} realization. \hat{w}_q is the value of \hat{w} for the q^{th} realization.

The standard deviation $\sigma(P)$ is computed simultaneously with P [40].

3.2 Estimation of the geometric sensitivities of power

The whole matrix of sensitivity of impacting power \mathbf{S} has a dimension of $n_{\mathcal{H}} \times n_{\vec{\pi}}$, where $n_{\mathcal{H}}$ is the number of heliostats and $n_{\vec{\pi}} = 6$ is the number of geometric parameters of each heliostat, referring to Fig.4. When the number of heliostats $n_{\mathcal{H}}$ becomes large, it will be very costly in computing time if we estimate them one by one.

Herein, we will build an efficient algorithm to estimate \mathbf{S} . The matrix of \mathbf{S} is composed of the vectors of sensitivities for each heliostat $\mathbf{S} \equiv [\vec{S}_i]$ (reminding the index i for i^{th} Heliostat in the field):

$$\vec{S}_i(\vec{\pi}) \equiv \begin{bmatrix} S_{i,1}(\vec{\pi}) \\ S_{i,2}(\vec{\pi}) \\ S_{i,3}(\vec{\pi}) \\ S_{i,4}(\vec{\pi}) \\ S_{i,5}(\vec{\pi}) \\ S_{i,6}(\vec{\pi}) \end{bmatrix}^T \quad (36)$$

Following Eq.27, each $S_{i,j}$ has 4 contributions. We defined the vectors of contributions as well as the vectors of sources similarly, and finally, we have:

$$\vec{S}_i = \vec{S}_i^{tar} + \vec{S}_i^{blo} + \vec{S}_i^{shad-b} + \vec{S}_i^{shad-f} \quad (37)$$

and

$$\vec{s}_i = \vec{s}_i^{tar} + \vec{s}_i^{blo} + \vec{s}_i^{shad-b} + \vec{s}_i^{shad-f}. \quad (38)$$

The contributions will then be the sum of captured sources respectively on the \mathcal{H} . The corresponding integral formulations are detailed in Appendix.B. The algorithm to estimate \mathbf{S} and its standard deviation $\sigma(\mathbf{S})$ is Algo.1.

Algorithm 1 Estimate \mathbf{S} and $\sigma(\mathbf{S})$

Input: Geometries of heliostats and receiver, $\vec{\omega}_c$
 $\triangleright \vec{\omega}_c$ characterizes the solar position (Eq.15)

Initialization: $i \leftarrow 0$

while $i < n_{\mathcal{H}}$ **do** $\triangleright n_{\mathcal{H}}$ number of heliostats

Estimate \vec{S}_i^{tar} and $\vec{\sigma}(\vec{S}_i^{tar})$ by Algo.3

Estimate \vec{S}_i^{blo} and $\vec{\sigma}(\vec{S}_i^{blo})$ by Algo.4

Estimate \vec{S}_i^{shad-b} and $\vec{\sigma}(\vec{S}_i^{shad-b})$ by Algo.6

Estimate \vec{S}_i^{shad-f} and $\vec{\sigma}(\vec{S}_i^{shad-f})$ by Algo.5

$\vec{S}_i \leftarrow \vec{S}_i^{tar} + \vec{S}_i^{blo} + \vec{S}_i^{shad-b} + \vec{S}_i^{shad-f}$

$\vec{\sigma}(\vec{S}_i) \leftarrow \vec{\sigma}(\vec{S}_i^{mat}) + \vec{\sigma}(\vec{S}_i^{blo}) + \vec{\sigma}(\vec{S}_i^{shad-b}) + \vec{\sigma}(\vec{S}_i^{shad-f})$

$i \leftarrow i + 1$

end while

Output: $\mathbf{S} \leftarrow [\vec{S}_i]$, $\sigma(\mathbf{S}) \leftarrow [\vec{\sigma}(\vec{S}_i)]$

In the following part of this section, we will discuss the estimation of each vector of contribution in Eq.37.

3.2.1 Contribution of the effect of targeting \vec{S}_i^{tar}

$S_{i,j}^{tar}$ is a component of \vec{S}_i^{tar} , estimated by the sum of the sources of targeting $\vec{s}_{i,j}^{tar}(\vec{\pi})$ arriving to the receiver. The corresponding integral formulation is yielded in Appendix.B and is separated into two parts, corresponding to the change of position (Fig.8) and the change of normal (Fig.9), noted $\vec{S}_i^{tar,spatial}$ and $\vec{S}_i^{tar,angular}$ respectively. The corresponding sources of sensitivities are separated by $\vec{s}_{i,j}^{tar,spatial}$ and $\vec{s}_{i,j}^{tar,angular}$ in Eq.25. Those sources correspond to the spatial gradient of intensity I and the angular gradient of I [33]. It is noted that the $\vec{\pi}_{i,4}$ and the $\vec{\pi}_{i,5}$ characterize the change of normal and also the

change of positions (because they are related to the rotations). In contrast, other parameters characterize only the change of position.

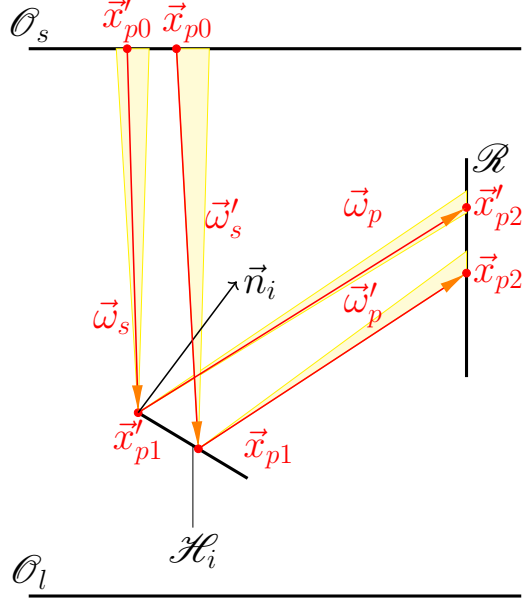


Figure 14: Algorithm to compute \bar{S}_i^{tar} . \bar{x}_{p1} is on the 4 borders of the heliostat $\partial\mathcal{H}_i$ having k as the index of the border, \bar{x}'_{p0} the first intersection starting by \bar{x}'_{p1} following $-\bar{\omega}_s$, \bar{x}'_{p2} the first intersection starting by \bar{x}'_{p1} following $\bar{\omega}_p$, $\bar{\omega}'_s$ the direction on the border of solar cone $\partial\Omega_s$, $\bar{\omega}'_p$ the direction of reflection of $\bar{\omega}'_s$, \bar{x}_{p0} the first intersection starting by \bar{x}_{p1} following $-\bar{\omega}'_s$ and \bar{x}_{p2} the first intersection starting by \bar{x}_{p1} following $\bar{\omega}'_p$. For each realization of estimating $\bar{S}_i^{tar,spatial}$, we sample \bar{x}'_{p1} and $\bar{\omega}_s$. If \bar{x}'_{p0} hits \mathcal{O}_s and \bar{x}'_{p2} hits \mathcal{R} we count \bar{w}_1 (Eq.42). For each realization of estimating $\bar{S}_i^{tar,angular}$, we sample \bar{x}_{p1} and $\bar{\omega}'_s$. If \bar{x}_{p0} hits \mathcal{O}_s and \bar{x}_{p2} hits \mathcal{R} we count \bar{w}_2 (Eq.43).

The integral formulation for estimating \bar{S}_i^{tar} is detailed in Eq. 39 and Eq. 40. Corresponding probability density functions are given in Eq. 41. In Eq. 40, k refers to the four sides of the squared heliostat.

$$\bar{S}_i^{tar}(\ddot{\mathbf{n}}) = \bar{S}_i^{tar,spatial}(\ddot{\mathbf{n}}) + \bar{S}_i^{tar,angular}(\ddot{\mathbf{n}}) \quad (39)$$

$$\left\{ \begin{array}{l} \bar{S}_i^{tar,spatial}(\ddot{\mathbf{n}}) = \sum_{k=1}^4 \int_{l_k} p_{X'}(\bar{x}'_{p1}) d\bar{x}'_p \int_{\Omega_s} p_{\Omega_s}(\bar{\omega}_s) d\bar{\omega}_s \\ \quad \{ \bar{w}_1 \mathcal{H}(\bar{x}'_{p0} \in \mathcal{O}_s) \mathcal{H}(\bar{x}'_{p2} \in \mathcal{R}) \} \\ \bar{S}_i^{tar,angular}(\ddot{\mathbf{n}}) = \int_{\mathcal{H}_i^+} p_{X_i}(\bar{x}_{p1}) d\bar{x}_p \int_{\partial\Omega_s} p_{\Omega'_s}(\bar{\omega}'_s) d\bar{\omega}'_s \\ \quad \{ \bar{w}_2 \mathcal{H}(\bar{x}_{p0} \in \mathcal{O}_s) \mathcal{H}(\bar{x}_{p2} \in \mathcal{R}) \} \end{array} \right. \quad (40)$$

where

$$p_{X_i}(\vec{x}_{p1}) = \frac{1}{\mathcal{S}_{\mathcal{H}_i^+}}; p_{X'}(\vec{x}'_{p1}) = \frac{1}{l_k}; p_{\Omega'_s}(\vec{\omega}'_s) = \frac{1}{2\pi} \quad (41)$$

$$\vec{w}_1 = \frac{\vec{s}_i^{\text{tar}, \text{spatial}}(\vec{x}_p, \vec{\omega}_p, \vec{\pi})}{p_{X'}(\vec{x}'_{p1})p_{\Omega_s}(\vec{\omega}_s)}; \quad (42)$$

$$\vec{w}_2 = \frac{\vec{s}_i^{\text{tar}, \text{angular}}(\vec{x}_p, \vec{\omega}_p, \vec{\pi})}{p_{X_i}(\vec{x}_{p1})p_{\Omega'_s}(\vec{\omega}'_s)}. \quad (43)$$

The notation and the Monte-Carlo ray-tracing algorithm are shown in Fig.14. See also Algo.3 for the complete algorithm and Appendix.C for the explicit expression of \vec{w}_1 and \vec{w}_2 .

3.2.2 Contribution of backward-blocking effect \vec{S}_i^{blo}

$S_{i,j}^{\text{blo}}$ is a component of \vec{S}_i^{blo} , estimated by the sum of the sources of backward-blocking $\vec{s}_{i,j}^{\text{blo}}(\vec{\pi})$ arriving to the receiver. The corresponding integral formulation is yielded in Appendix.B.

Unlike the source of targeting, the evolution of $\vec{\pi}_{i,j}$ has no effects on the change of normal of the reflected intensity (Fig.15). Intensity is reflected following $\vec{n}_{i'}$ on $\mathcal{H}_{i'}^+$, while $\vec{\pi}_{i,j}$ characterizes the heliostat \mathcal{H}_i . Therefore, $\vec{s}_{i,j}^{\text{blo}}$ is only about the change of position.

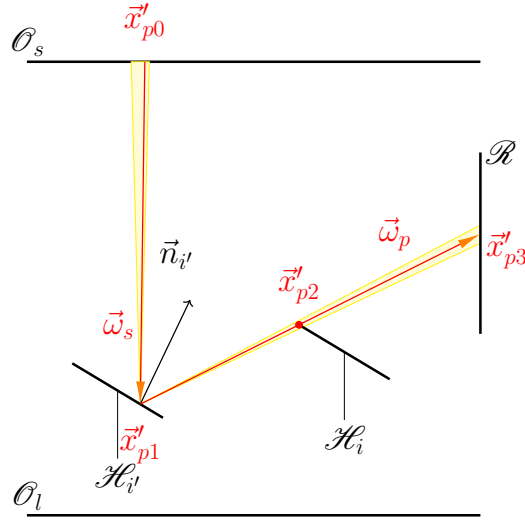


Figure 15: Algorithm to compute \vec{S}_i^{blo} . \vec{x}'_{p1} is the first intersection starting by \vec{x}'_{p2} , following $-\vec{\omega}_p$, \vec{x}'_{p0} the first intersection starting by \vec{x}'_{p1} following $-\vec{\omega}_s$, \vec{x}'_{p3} the first intersection starting by \vec{x}'_{p1} following $\vec{\omega}_p$. For each realization of estimating \vec{S}_i^{blo} , we sample \vec{x}'_{p2} and $\vec{\omega}_s$, and we calculate $\vec{\omega}_p$. If \vec{x}'_{p0} hits O_s , \vec{x}'_{p1} hits $\mathcal{H}_{i'}$ and \vec{x}'_{p2} hits \mathcal{R} we count \vec{w}_3 .

Seeing Fig.15 for the ray-tracing algorithm, the integral formulation for estimating \vec{S}_i^{blo} is as following:

$$\vec{S}_i^{blo}(\vec{\pi}) = \sum_{i'=1}^{n_{\mathcal{H}}, i' \neq i} \sum_{k=1}^4 \int_{l_k} p_{X'}(\vec{x}'_{p2}) d\vec{x}'_{p2} \int_{\Omega_s} p_{\Omega_s}(\vec{\omega}_s) d\vec{\omega}_s \{ \vec{w}_3 \mathcal{H}(\vec{x}'_{p0} \in \mathcal{O}_s) \mathcal{H}(\vec{x}'_{p1} \in \mathcal{H}_i^+) \mathcal{H}(\vec{x}'_{p3} \in \mathcal{R}) \} \quad (44)$$

where

$$\vec{w}_3 = \frac{\vec{s}_i^{blo}(\vec{x}'_{p2}, \vec{\omega}_p, \vec{\pi})}{p_{X'}(\vec{x}'_{p2}) p_{\Omega_s}(\vec{\omega}_s)} \quad (45)$$

with $n_{\mathcal{H}}$ the number of heliostats in the field.

Moreover, the blocked heliostat $\mathcal{H}_{i'}$ can be all other heliostats except \mathcal{H}_i in the heliostats field. In order to capture all the sources $\vec{s}_{i,j}^{blo}(\vec{\pi}_{i,j})$, we need to proceed ray-tracing test for all other heliostats except \mathcal{H}_i in the field to detect the blocking effect. However, most of them will not be blocked by \mathcal{H}_i since the distance between the two heliostats is large. In order to accelerate and optimize the algorithm, we will proceed with the ray-tracing tests on the heliostats, of which the distance to \mathcal{H}_i is within a limited length. This length is defined as l_d . See Algo.4 for the complete algorithm and Appendix.C for the explicit expression of \vec{w}_3 .

3.2.3 Contribution of forward-shadowing $\vec{S}_{i,j}^{shad-f}$

$S_{i,j}^{shad-f}$ is a component of $\vec{S}_{i,j}^{shad-f}$, estimated by the sum of the sources of forward-shadowing $\vec{s}_{i,j}^{shad-f}(\vec{\pi})$ arriving to the receiver. The corresponding integral formulation is yielded in Appendix.B.

Seeing the ray-tracing algorithms on Fig.16, \vec{S}_i^{shad-f} can be estimated by the following integral formulation:

$$\vec{S}_i^{shad-f}(\vec{\pi}) = \sum_{k=1}^4 \int_{l_k} p_{X'}(\vec{x}'_{p1}) d\vec{x}'_{p1} \int_{\Omega_s} p_{\Omega_s}(\vec{\omega}_s) d\vec{\omega}_s \{ \vec{w}_4 \mathcal{H}(\vec{x}'_{p0} \in \mathcal{O}_s) \mathcal{H}(\vec{x}'_{p2} \in \mathcal{H}^+) \mathcal{H}(\vec{x}'_{p3} \in \mathcal{R}) \}, \quad (46)$$

where

$$\vec{w}_4 = \frac{\vec{s}_i^{shad-f}(\vec{x}'_{p1}, \vec{\omega}_p, \vec{\pi})}{p_{X'}(\vec{x}'_{p1}) p_{\Omega_s}(\vec{\omega}_s)}. \quad (47)$$

See also Algo.5 for the complete algorithm and Appendix.C for the explicit expression of \vec{w}_4 .

3.2.4 Contribution of backward-shadowing effect \vec{S}_i^{shad-b}

$S_{i,j}^{shad-b}$ is a component of \vec{S}_i^{shad-b} , estimated by the sum of the sources of backward-shadowing $\vec{s}_{i,j}^{shad-b}(\vec{\pi})$ arriving to the receiver. The corresponding integral formulation is yielded in Appendix.B. Similar to the targeting effect, the evolution of $\vec{\pi}_{i,j}$ might have two possible impacts on the heliostat \mathcal{H}_i : the change

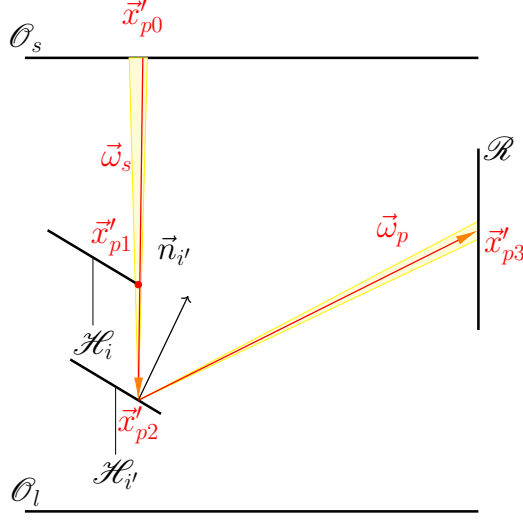


Figure 16: Algorithm to compute \vec{S}_i^{shad-f} . \vec{x}'_{p0} is the first intersection starting by \vec{x}'_{p1} , following $-\vec{\omega}_s$, \vec{x}'_{p2} the first intersection starting by \vec{x}'_{p1} following $\vec{\omega}_s$, \vec{x}'_{p3} the first intersection starting by \vec{x}'_{p2} following $\vec{\omega}_p$. For each realization of estimating \vec{S}_i^{blo} , we sample \vec{x}'_{p1} and $\vec{\omega}_s$, and we calculate $\vec{\omega}_p$. $\vec{\omega}_p$ is reflected following the normal $\vec{n}_{i'}$ which is the normal of \mathcal{H}_i . If \vec{x}'_{p0} hits \mathcal{O}_s , \vec{x}'_{p2} hits \mathcal{H}_i^+ and \vec{x}'_{p3} hits \mathcal{R} we count \vec{w}_4 .

of position and the change of normal, impacting the backward-shadowing effect. Therefore, the contribution \vec{S}_i^{shad-b} can be divided by two parts: $\vec{S}_i^{shad-b,spatial}$ for the change of position and $\vec{S}_i^{shad-b,angular}$ for the change of normal. Also, the sources $\vec{s}_{i,j}^{shad-b,spatial}$ are divided by two parts respectively: $\vec{s}_{i,j}^{shad-b,spatial}$ and $\vec{s}_{i,j}^{shad-b,angular}$ in Eq.26. They correspond to the spatial and the angular gradient of intensity I on the reflecting surface of the heliostat \mathcal{H}_i^+ [33].

Seeing Fig.10a and Fig.10b, these two gradients (spatial and angular) are both originated from the borders of another heliostat (from point \vec{x}'_{p1} in Fig.17).

Seeing the algorithm of ray-tracing in Fig17, \vec{S}_i^{shad-b} can be estimated through the following integral formulation:

$$\vec{S}_i^{shad-b}(\vec{\pi}) = \sum_{k=1}^{4 \times n_{\mathcal{H}}} \int_{l_k} p_{X'}(\vec{x}'_{p1}) d\vec{x}'_{p1} \int_{\Omega_s} p_{\Omega_s}(\vec{\omega}_s) d\vec{\omega}_s \{(\vec{w}_5 + \vec{w}_6) \mathcal{H}(\vec{x}'_{p0} \in \mathcal{O}_s) \mathcal{H}(\vec{x}'_{p2} \in \mathcal{H}_i^+) \mathcal{H}(\vec{x}'_{p3} \in \mathcal{R})\}, \quad (48)$$

where

$$\vec{w}_5 = \frac{\vec{s}_i^{shad-b,spatial}(\vec{x}'_{p1}, \vec{\omega}_p, \vec{\pi})}{p_{X'}(\vec{x}'_{p1}) p_{\Omega_s}(\vec{\omega}_s)}; \quad (49)$$

$$\vec{w}_6 = \frac{\vec{s}_i^{shad-b,angular}(\vec{x}'_{p1}, \vec{\omega}_p, \vec{\pi})}{p_{X'}(\vec{x}'_{p1}) p_{\Omega_s}(\vec{\omega}_s)}. \quad (50)$$

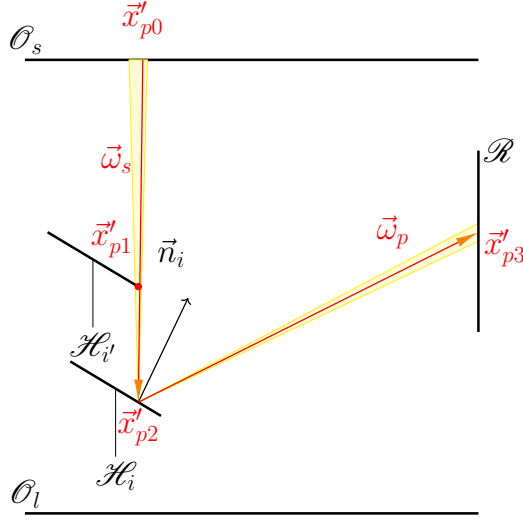


Figure 17: Algorithm to compute \vec{S}_i^{shad-b} . \vec{x}'_{p0} is the first intersection starting by \vec{x}'_{p1} , following $-\vec{\omega}_s$, \vec{x}'_{p2} the first intersection starting by \vec{x}'_{p1} following $\vec{\omega}_s$, \vec{x}'_{p3} the first intersection starting by \vec{x}'_{p2} following $\vec{\omega}_p$, $\vec{t}'_{i,k}$ the vector of circulation on the shadowing heliostat $\mathcal{H}_{i'}$, l_{shad-b} the length of the optical path between \vec{x}'_{p1} and \vec{x}'_{p2} . For each realization of estimating \vec{S}_i^{blo} , we sample \vec{x}'_{p1} and $\vec{\omega}_s$, and we calculate $\vec{\omega}_p$. $\vec{\omega}_p$ is reflected following the normal \vec{n}_i which is the normal of \mathcal{H}_i . If \vec{x}'_{p0} hits O_s , \vec{x}'_{p2} hits \mathcal{H}_i^+ and \vec{x}'_{p3} hits \mathcal{R} we count $\vec{w}_5 + \vec{w}_6$.

Similar to the backward-blocking effect, $\mathcal{H}_{i'}$ can be all other heliostats except \mathcal{H}_i itself in the heliostats field. In order to detect all backward-shadowing effects, we need to proceed with ray-tracing tests for all the borders of all heliostats in the field except the borders of \mathcal{H}_i ($4 \times (n_{\mathcal{H}} - 1)$ in total where $n_{\mathcal{H}}$ is the number of heliostats in the field). However, most of them will not create shadows on \mathcal{H}_i since they are too far from each other. In order to accelerate and optimize the algorithm, we will only proceed with the ray-tracing tests for the heliostats, of which the distance to \mathcal{H}_i is within l_d . See also Algo.6 for the complete algorithm and Appendix.C for the explicit expression of \vec{w}_5 and \vec{w}_6 .

4 Results, validations, and comparisons

In this section, we will proceed with the following:

1. Validations of our method by finite difference method using four examples.
2. A comparison of the finite difference method with our method in calculating time.

4.1 Validations

We will here proceed with four simple examples (see Fig.18) where we apply our method and finite difference method for validation purposes. The sensitivities of \mathcal{H}_1 are calculated and results are shown in Table.2, 3, 4 and 5. In case 1, only

the spillage effect is detected. In case 2, the blocking effect is detected. In case 3, the backward-shadowing effect is detected. In case 4, the forward-shadowing effect is detected. The estimation results by our method are validated by the finite difference method, which will be discussed in the following subsection.

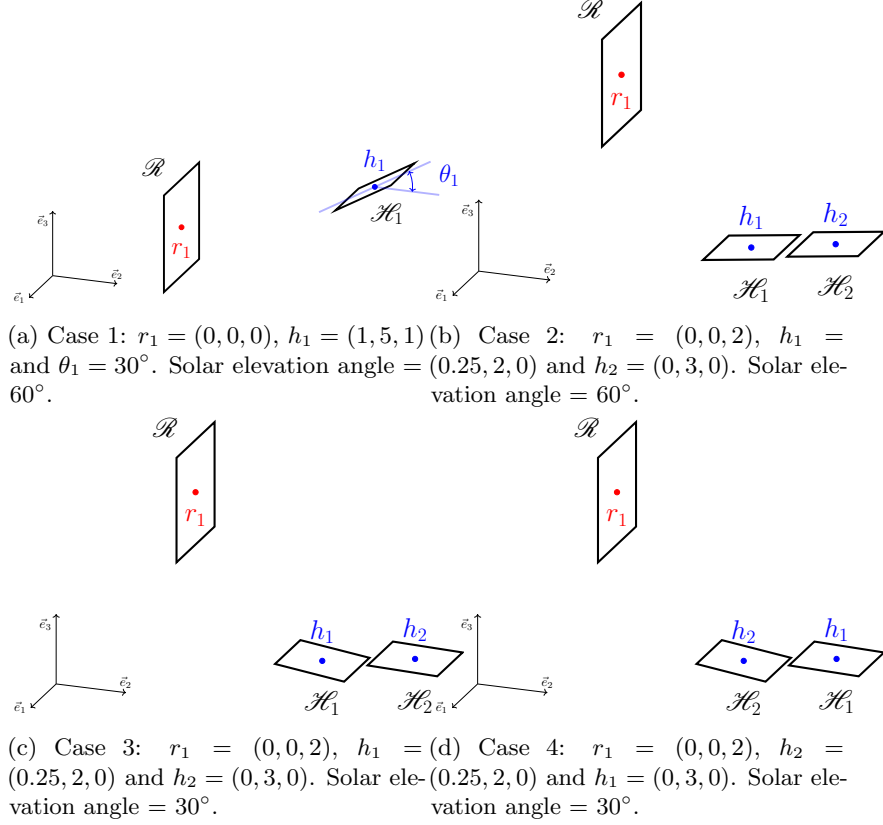


Figure 18: The receiver \mathcal{R} is a rectangular with lengths of 1.50 m and r_1 is its geometric center. The heliostats \mathcal{H}_1 and \mathcal{H}_2 are two rectangles with lengths of 1 m and h_1, h_2 are their geometric centers respectively. In case 1, θ_1 is the horizontal angle of \mathcal{H}_1 . In case 2, 3 and 4, the heliostat \mathcal{H}_1 and \mathcal{H}_2 point to r_1 according to the solar elevation angle.

4.1.1 Approximation by finite difference method

The finite difference method is a standard method to approximate the sensitivities. When P is derivable around $\tilde{\pi}_{i,j}$:

$$S_{i,j} = \lim_{\epsilon \rightarrow 0} \frac{P(\tilde{\pi}_{i,j} + \epsilon) - P(\tilde{\pi}_{i,j} - \epsilon)}{2\epsilon}. \quad (51)$$

The finite difference method approximates $S_{i,j}$ by giving a non-zero fixed value to ϵ . We note the result of approximation as $\tilde{S}_{i,j}$:

$$S_{i,j} \approx \frac{P(\tilde{\pi}_{i,j} + \Delta\tilde{\pi}_{i,j}) - P(\tilde{\pi}_{i,j} - \Delta\tilde{\pi}_{i,j})}{2\Delta\tilde{\pi}_{i,j}} \equiv \tilde{S}_{i,j}. \quad (52)$$

| unit | W/m | W/m | W/m | W/rad | W/rad | W/m |
|----------------------------|-------------------------|-------------------------|-------------------------|--------------------|-------------------------|-------------------------|
| j | 1 | 2 | 3 | 4 | 5 | 6 |
| $S_{1,j}^{star,spatial}$ | -4.56 | 244.82×10^{-3} | -125.12 | 54.24 | -2.02 | 33.45 |
| $S_{1,j}^{star,angular}$ | 0.00 | 0.00 | 0.00 | 1.14×10^3 | -10.37 | 0.00 |
| $S_{1,j}^{blo}$ | 0.00 | 0.00 | 0.00 | 0.00 | 0.00 | 0.00 |
| $S_{1,j}^{shad-b,spatial}$ | 0.00 | 0.00 | 0.00 | 0.00 | 0.00 | 0.00 |
| $S_{1,j}^{shad-b,angular}$ | 0.00 | 0.00 | 0.00 | 0.00 | 0.00 | 0.00 |
| $S_{1,j}^{shad-f}$ | 0.00 | 0.00 | 0.00 | 0.00 | 0.00 | 0.00 |
| $\tilde{S}_{1,j}$ | -4.56 | 244.82×10^{-3} | -125.12 | 1.20×10^3 | -12.39 | 33.45 |
| $\sigma(\tilde{S}_{1,j})$ | 47.41×10^{-3} | 876.00×10^{-6} | 331.02×10^{-3} | 2.19 | 382.67×10^{-3} | 106.14×10^{-3} |
| $\tilde{S}_{1,j}$ | -4.50 | 244.00×10^{-3} | -124.91 | 1.19×10^3 | -12.27 | 33.41 |
| $\sigma(\tilde{S}_{1,j})$ | 235.23×10^{-3} | 235.23×10^{-3} | 238.22×10^{-3} | 2.38 | 2.35 | 236.04×10^{-3} |

Table 2: Validation - Case 1: 10^6 realizations on each border and 10^8 realizations on the surface for an estimation of $S_{1,j}$ and 10^7 realizations for each estimation of P when approximating $\tilde{S}_{1,j}$ by finite difference method.

| unit | W/m | W/m | W/m | W/rad | W/rad | W/m |
|----------------------------|-------------------------|-------------------------|-------------------------|---------|-------------------------|-------------------------|
| j | 1 | 2 | 3 | 4 | 5 | 6 |
| $S_{1,j}^{star,spatial}$ | -793.35 | 143.71×10^{-3} | 141.22×10^{-3} | 456.62 | 356.02×10^{-3} | 991.76 |
| $S_{1,j}^{star,angular}$ | 0.00 | 0.00 | 0.00 | -912.74 | -463.55 | 0.00 |
| $S_{1,j}^{blo}$ | 139.39 | -277.29 | -415.94 | -188.09 | 14.84 | -234.30 |
| $S_{1,j}^{shad-b,spatial}$ | 0.00 | 0.00 | 0.00 | 0.00 | 0.00 | 0.00 |
| $S_{1,j}^{shad-b,angular}$ | 0.00 | 0.00 | 0.00 | 0.00 | 0.00 | 0.00 |
| $S_{1,j}^{shad-f}$ | 0.00 | 0.00 | 0.00 | 0.00 | 0.00 | 0.00 |
| $\tilde{S}_{1,j}$ | -653.96 | -277.15 | -415.80 | -644.22 | -448.36 | 757.46 |
| $\sigma(\tilde{S}_{1,j})$ | 270.41×10^{-3} | 890.09×10^{-3} | 1.03 | 13.81 | 2.08 | 643.34×10^{-3} |
| $\tilde{S}_{1,j}$ | -654.25 | -277.20 | -415.90 | -640.00 | -450.50 | 757.50 |
| $\sigma(\tilde{S}_{1,j})$ | 180.35×10^{-3} | 181.87×10^{-3} | 181.38×10^{-3} | 18.23 | 1.82 | 1.82 |

Table 3: Validation - Case 2: 10^6 realizations on each border and 10^9 realizations on the surface for an estimation of $S_{1,j}$ and 10^9 realizations for each estimation of P when approximating $\tilde{S}_{1,j}$ by finite difference method.

Practically, the approximation of $\tilde{S}_{i,j}$ requires estimating P twice. Since the impacting power P is estimated by the Monte-Carlo method, its statistical standard deviation $\sigma(P)$ is also estimated at the same time [40]. When approximating $\tilde{S}_{i,j}$, its standard deviation $\sigma(\tilde{S}_{i,j})$ can be obtained [23]:

$$\sigma(\tilde{S}_{i,j}) \approx \frac{\sigma(P(\tilde{\pi}_{i,j} + \Delta\tilde{\pi}_{i,j})) + \sigma(P(\tilde{\pi}_{i,j} - \Delta\tilde{\pi}_{i,j}))}{2\Delta\tilde{\pi}_{i,j}}. \quad (53)$$

The major drawback of the finite difference method is that the related standard deviation $\sigma(\tilde{S}_{i,j})$ is hard to control[23] and tends to infinity as $\Delta\tilde{\pi}_{i,j}$ tends to zero.

4.2 Comparison with the finite difference method

In this section, we will apply and discuss the algorithms previously introduced in the context of a functioning solar tower station: Sierra SunTower [34]. This case study has been chosen since our sensitivity model was developed for flat heliostats.

This solar tower station is located in Mojave Desert, California, at a latitude of 34.7° . It consists of 2 solar towers, each with north and south heliostat subfields[34].

The heliostat field and the two towers are symmetrically distributed. Therefore, we only focus on the field on the southwest side and its related tower,

| unit | W/m | W/m | W/m | W/rad | W/rad | W/m |
|----------------------------|-------------------------|-------------------------|-------------------------|--------------------|--------|-------------------------|
| j | 1 | 2 | 3 | 4 | 5 | 6 |
| $S_{1,j}^{tar,spatial}$ | -236.19 | -531.19 | -530.35 | -493.65 | 35.84 | 801.24 |
| $S_{1,j}^{tar,angular}$ | 0.00 | 0.00 | 0.00 | 1.64×10^3 | 137.89 | 0.00 |
| $S_{1,j}^{shlo}$ | 0.00 | 0.00 | 0.00 | 0.00 | 0.00 | 0.00 |
| $S_{1,j}^{shad-b,spatial}$ | 0.00 | 155.41 | 1.18×10^3 | -461.94 | -19.41 | 12×10^{-6} |
| $S_{1,j}^{shad-b,angular}$ | 0.00 | 0.00 | 0.00 | -200.32 | -1.56 | 0.00 |
| $S_{1,j}^{shad-f}$ | 0.00 | 0.00 | 0.00 | 0.00 | 0.00 | 0.00 |
| $\tilde{S}_{1,j}$ | -236.19 | -375.79 | 650.09 | 479.69 | 152.76 | 801.24 |
| $\sigma(S_{1,j})$ | 496.41×10^{-3} | 427.22×10^{-3} | 1.02 | 11.88 | 1.53 | 393.25×10^{-3} |
| $\tilde{S}_{1,j}$ | -236.00 | -376.00 | 649.50 | 490.00 | 150.00 | 800.50 |
| $\sigma(\tilde{S}_{1,j})$ | 780.28×10^{-3} | 771.28×10^{-3} | 770.40×10^{-3} | 7.72 | 7.72 | 773.85×10^{-3} |

Table 4: Validation - Case 3: 10^6 realizations on each border and 10^9 realizations on the surface for an estimation of $S_{1,j}$ and 10^9 realizations for each estimation of P when approximating $\tilde{S}_{1,j}$ by finite difference method.

| unit | W/m | W/m | W/m | W/rad | W/rad | W/m |
|----------------------------|-------------------------|-------------------------|-------------------------|--------------------|-------------------------|-------------------------|
| j | 1 | 2 | 3 | 4 | 5 | 6 |
| $S_{1,j}^{tar,spatial}$ | -1.29×10^{-3} | -2.10×10^{-3} | -2.31×10^{-3} | -849.47 | 242.46×10^{-3} | 1.06×10^3 |
| $S_{1,j}^{tar,angular}$ | 0.00 | 0.00 | 0.00 | 1.69×10^3 | -88.94×10^{-3} | 0.00 |
| $S_{1,j}^{shlo}$ | 0.00 | 0.00 | 0.00 | 0.00 | 0.00 | 0.00 |
| $S_{1,j}^{shad-b,spatial}$ | 0.00 | 0.00 | 0.00 | 0.00 | 0.00 | 0.00 |
| $S_{1,j}^{shad-b,angular}$ | 0.00 | 0.00 | 0.00 | 0.00 | 0.00 | 0.00 |
| $S_{1,j}^{shad-f}$ | -68.35 | 375.08 | -649.65 | -318.62 | 17.21 | -232.07 |
| $\tilde{S}_{1,j}$ | -68.35 | 375.08 | -649.66 | 523.12 | 17.37 | 823.17 |
| $\sigma(S_{1,j})$ | 181.08×10^{-3} | 220.47×10^{-3} | 382.90×10^{-3} | 10.45 | 973.89×10^{-3} | 206.71×10^{-3} |
| $\tilde{S}_{1,j}$ | -68.50 | 375.00 | -649.50 | 530.00 | 15.00 | 823.00 |
| $\sigma(\tilde{S}_{1,j})$ | 771.70×10^{-3} | 771.28×10^{-3} | 770.40×10^{-3} | 7.72 | 7.72 | 771.70×10^{-3} |

Table 5: Validation - Case 4: 10^6 realizations on each border and 10^9 realizations on the surface for an estimation of $S_{1,j}$ and 10^9 realizations for each estimation of P when approximating $\tilde{S}_{1,j}$ by finite difference method.

which includes 6090 flat heliostats. It is easy to extend the calculation for the whole field in the south (including 12180 heliostats). However, extra efforts are needed for the field on the north side since the towers' shadows will impact the sensitivities.

Table.6 shows the geometric parameters of the radiative system, as well as the solar positions for the summer solstice.

| Characteristic | Value |
|--|--|
| Overall north-south length | 95 [m] |
| Overall east-west length | 175 [m] |
| Distance between the tower and the first row of heliostats | 12.5 [m] |
| Number of heliostats per column | 58 |
| Number of heliostats per row | 105 |
| Size of heliostats | 1.067×1.067 [m ²] |
| Height of the centre of receiver | 50 [m] |
| Size of receiver | 4×4 [m ²] |
| Zenith angle for the summer solstice at solar noon | 79° |

Table 6: Geometric configuration of the system[34]

The present work focuses on the optical performance (the impacting power P). It is assumed that:

1. The sun's position is fixed (solar noon for the summer solstice)
2. Incoming Direct Normal Intensity (DNI) is considered homogeneous for the whole heliostat field (DNI = 1000W/m²).

The incoming power, $P(\vec{\pi})$ and its derivatives $\mathcal{S}(\vec{\pi})$ towards geometric parameters $\vec{\pi} \equiv [\vec{\pi}_{i,j}]$ are estimated. It is reminded that i refers to the i^{th} heliostat ($i \in \{1, 2, \dots, 6090\}$) and j to one of the six geometric parameters ($j \in \{1, 2, \dots, 6\}$) as shown on Fig.4.

Results have already been shown at the beginning of this article (Fig.2). It is noted that the accuracy of the simulation depends on the number of Monte Carlo realizations. Each Monte-Carlo realization consists of the corresponding sampling process and the ray-tracing tests described in Section.3.

When we focus on one parameter of one heliostat in the field (for example, the size of the 5297th heliostat: $\vec{\pi}_{5297,6}$), it has a tinny impact on the total impacting power P . It causes a poor convergence performance when applying the finite difference method, as shown in Table.7. Compared to our method, the method of approximation by finite difference takes much more time to converge because the choice of $\Delta\vec{\pi}$ enormously impacts the convergence rate and the precision for the approximation method of finite difference. In contrast, our method of estimation avoids this choice. These calculations are run parallelly in an ordinary laptop¹, and our method converges in 0.188s. According to [40], to reduce ten times the standard deviation of a Monte-Carlo estimation, approximately 100 times the calculation time is needed. In this application case, the approximation of the

¹4 CPUs of i5 Intel™, 8th generation

finite difference method will then spend approximately 2×10^{11} more times of calculating time to attend the same order of standard deviation of our method.

Last but not least, it is found that in Table.2, Table.3, Table.4 and Table.5, the advantage of our method in convergence performance is not that significant compared to the finite difference method. We have the following comments:

1. The four cases are dedicated to validation purposes. Therefore, the geometries are relatively simple compared to a functioning SPT system. However, the finite difference method will become impracticable when the geometries become more complex.
2. Even with simple geometries, the standard derivation of the finite difference method ($\sigma(\tilde{S}_{i,j})$) is hard to be controlled. It is strongly dependent on the value of $\Delta\tilde{\pi}_{i,j}$ chosen in Eq.52 and Eq.53.
3. The derivation related to the discretization can not be handled for the finite difference method. It is also largely related to the choice of $\Delta\tilde{\pi}$ in Eq.52 and Eq.53. However, our method can handle the statistical standard derivation. We avoid the derivation related to the discretization and the choice of $\Delta\tilde{\pi}_{i,j}$.

| Finite difference method | Value | standard deviation | calculation time |
|--|--------------|--------------------|------------------|
| $P(\tilde{\pi}_{5297,6} - \Delta\tilde{\pi}_{5297,6})$ | 3231.62[w] | 0.0389[w] | 272.5[s] |
| $P(\tilde{\pi}_{5297,6} + \Delta\tilde{\pi}_{5297,6})$ | 3231.85[w] | 0.0389[w] | 272.5[s] |
| $\tilde{S}_{5297,6}(\tilde{\pi}_{5297,6})$ | 1.15[w/m] | 0.389[w/m] | 545[s] |
| Our method | Value | standard deviation | calculation time |
| $S_{5297,6}(\tilde{\pi}_{5297,6})$ | 1.14974[w/m] | 0.000041[w/m] | 0.188[s] |

Table 7: $\tilde{\pi}_{5297,6}$ is originally equal to 1.067 (see Table.6), while herein, a reasonable value of $\Delta\tilde{\pi}_{5297,6}$ is chosen: $\Delta\tilde{\pi}_{5297,6} = 0.1[m]$. Two estimations of impacting power ($P(\tilde{\pi}_{5297,6} - \Delta\tilde{\pi}_{5297,6})$ and $P(\tilde{\pi}_{5297,6} + \Delta\tilde{\pi}_{5297,6})$) are realized following Algo.2 (10^9 Monte-Carlo realizations) . The sensitivity of power $\tilde{S}_{5297,6}$ is approximated based on these two estimations. Also, the sensitivity of power $S_{5297,6}$ is estimated following Algo.1 (10^4 Monte-Carlo realizations for each border of the heliostats).

5 Conclusion

We have presented general models for the intensity I and the sensitivity of intensity $s_{i,j}$ in a radiative system of an SPT system, as well as the complete algorithms for estimating the matrix of sensitivity of power \mathbf{S} . These algorithms are validated by the finite difference method using four typical examples. Since the sensitivity of a heliostat of a geometric parameter $S_{i,j}$ is estimated by the accumulation of four contributions: $S_{i,j}^{tar}$, $S_{i,j}^{blo}$, $S_{i,j}^{shad-b}$ and $S_{i,j}^{shad-f}$, the contributions of different physical events to the sensitivity $S_{i,j}$ in an SPT system (blocking, shadowing, spillage) can be analyzed in detail. After that, an actual

functioning SPT system was used as a test-case study. Firstly, a comparison of computing time was made for estimating sensitivity by our method and its approximation by the finite difference method. Secondly, the matrix of sensitivity of power \mathbf{S} was calculated. Engineers can benefit from this information on sensitivities to optimize the optical design and the aiming strategy for the SPT system. Last but not least, this work makes the integration of gradient-based optimizations for the optical system in an SPT becomes possible. However, the sensitivity model developed in the present paper is only applied to a field of flat heliostats. Thus, a promising perspective would be to extend this model to curved heliostats.

This work received financial support from the from Region Occitanie and the SOLSTICE laboratory of Excellence (ANR-10-LABX-22-01).

A Boundary conditions of geometric sensitivities for a heliostat

In this work, a heliostat is modeled by two surfaces without thickness: the reflecting surface \mathcal{H}_i^+ and the rearward surface \mathcal{H}_i^- .

Based on the general model in[33], the boundary condition of geometric sensitivities for a cold, specular mirror with homogeneous reflectivity is developed, where $I(\vec{x}_p, \vec{\omega}_p, \vec{\pi})$ and $I(\vec{x}_p, \vec{\omega}_s, \vec{\pi})$ are spatially and angularly smooth:

$$\begin{aligned}
s_{i,j}(\vec{x}_p, \vec{\omega}_p, \vec{\pi}) = & -\partial_{1, \vec{v}_{i,j}} I(\vec{x}_p, \vec{\omega}_p, \vec{\pi}) \\
& + \rho \partial_{1, \vec{v}_{i,j}} I(\vec{x}_p, \vec{\omega}_s, \vec{\pi}) \\
& - \rho \partial_R^{\vec{a}} I(\vec{x}_p, \vec{\omega}_s, \vec{\pi}) \\
& + \rho \partial_R^{\vec{a}'} I(\vec{x}_p, \vec{\omega}_s, \vec{\pi}) \\
& + \rho s_{i,j}(\vec{x}_p, \vec{\omega}_s, \vec{\pi})
\end{aligned} \tag{54}$$

where $\partial_{1, \vec{v}_{i,j}}$ is the operator for spatial gradient following the vector $\vec{v}_{i,j}$ which are the velocity of deformation (yielded in Appendix.D), $\partial_R^{\vec{a}}$ the operator for angular gradient following the vector of rotation \vec{a} , and \vec{a}' the reflected vector of $-\vec{a}$ on \mathcal{H}_i^+ [33]. However, when we model the reflecting surface \mathcal{H}_i^+ , $I(\vec{x}_p, \vec{\omega}_p, \vec{\pi})$ is spatially discontinued because the heliostat has 4 edges and $I(\vec{x}_p, \vec{\omega}_s, \vec{\pi})$ can be angularly discontinued (when backward-shadowing occurs, see Fig.10b).

In [33], the discontinuity of spatial gradient and angular gradient of intensity I are studied. The boundary condition of \mathcal{H}_i^+ can then be yielded. Furthermore, in this work, we classify the different sources of sensitivity based on the background of CSP applications:

$$\begin{aligned}
s_{i,j}(\vec{x}_p, \vec{\omega}_p, \vec{\pi}) = & \hat{s}_{i,j}^{tar}(\vec{x}_p, \vec{\omega}_p, \vec{\pi}) + \hat{s}_{i,j}^{blo}(\vec{x}_p, \vec{\omega}_p, \vec{\pi}) \\
& + \hat{s}_{i,j}^{shad-b}(\vec{x}_p, \vec{\omega}_p, \vec{\pi}) + \rho s_{i,j}(\vec{x}_p, \vec{\omega}_s, \vec{\pi}).
\end{aligned} \tag{55}$$

$\hat{s}_{i,j}^{tar}$ is separated into the source $\hat{s}_{i,j}^{tar,spatial}$ on the border of heliostat $\partial \mathcal{H}_i^+$ and the source $\hat{s}_{i,j}^{tar,angular}$ on the surface \mathcal{H}_i^+ : $\hat{s}_{i,j}^{tar} = \hat{s}_{i,j}^{tar,spatial} + \hat{s}_{i,j}^{tar,angular}$, where:

$$\hat{s}_{i,j}^{tar,spatial}(\vec{x}_p, \vec{\omega}_p, \vec{\pi}) = -(\vec{\omega}_p \times \vec{v}_{i,j}) \cdot \vec{t}_{i,k} \rho I(\vec{x}_p, \vec{\omega}_s, \vec{\pi}) \tag{56}$$

and

$$\begin{aligned} \hat{s}_{i,j}^{tar,angular}(\vec{x}_p, \vec{\omega}_p, \vec{\pi}) &= -\rho \partial_{\vec{R}}^{\vec{a}} I(\vec{x}_p, \vec{\omega}_s, \vec{\pi}) \\ &\quad + \rho \partial_{\vec{R}}^{\vec{a}'} I(\vec{x}_p, \vec{\omega}_s, \vec{\pi}). \end{aligned} \quad (57)$$

$\vec{t}_{i,k}$ are the vectors of circulation of \mathcal{H}_i^+ , depending on \vec{x}_p , see Fig.19.

When the backward-shadowing does not occur, the angular gradient in Eq.57 will be the angular derivative of the boundary condition of \mathcal{O}_s (previously defined in Eq.15, which is the Pill-box sun shape model). The development is straightforward, and they are the sources on the border of the solar cone $\partial\Omega_s$:

$$\partial_{\vec{R}}^{\vec{a}} I(\vec{x}_p, \vec{\omega}_s, \vec{\pi}) = I_0(\vec{\omega}_s \times \vec{a}) \cdot \vec{\omega}_c \mathcal{H}(hit_b \in \mathcal{O}_s) \quad (58)$$

$$\partial_{\vec{R}}^{\vec{a}'} I(\vec{x}_p, \vec{\omega}_s, \vec{\pi}) = I_0(\vec{\omega}_s \times \vec{a}') \cdot \vec{\omega}_c \mathcal{H}(hit_b \in \mathcal{O}_s) \quad (59)$$

where $\mathcal{H}(hit_b \in \mathcal{O}_s)$ corresponds to a backward ray-tracing test which will be true if the direction of $-\vec{\omega}_s$ starting from \vec{x}_p is not shadowed by other heliostats in the field.

$\hat{s}_{i,j}^{blo}$ is the source on the border of heliostat $\partial\mathcal{H}_i^+$:

$$\hat{s}_{i,j}^{blo}(\vec{x}_p, \vec{\omega}_p, \vec{\pi}) = (\vec{\omega}_p \times \vec{v}_{i,j}) \cdot \vec{t}_{i,k} I(\vec{x}_p, \vec{\omega}_p, \vec{\pi}) \quad (60)$$

When backward-shadowing effect occurs, \mathcal{H}_i^+ is shadowed by another heliostat $\mathcal{H}_{i'}^+$, a spatial gradient exists on the surface of \mathcal{H}_i^+ (Fig.10a). An angular gradient exists within the solar cone Ω_s (Fig.10b). Furthermore, in our case, these sources on the surface of \mathcal{H}^+ and within the cone Ω_s all come from the border of the shadowing heliostat $\partial\mathcal{H}_{i'}^+$.

Following the models of spatial gradient and angular gradient in [33], the source $\hat{s}_{i,j}^{shad-b}$ is on the borders of all heliostats in the field except the heliostat \mathcal{H}_i , which is $\partial\mathcal{H}_{i'}^+$, $i' \neq i$. Similar to the source of targeting, we separate the source $\hat{s}_{i,j}^{shad-b}$ by $\hat{s}_{i,j}^{shad-b,spatial}$ and $\hat{s}_{i,j}^{shad-b,angular}$:

$$\begin{aligned} \hat{s}_{i,j}^{shad-b}(\vec{x}_p, \vec{\omega}_p, \vec{\pi}) &= \hat{s}_{i,j}^{shad-b,spatial}(\vec{x}_p, \vec{\omega}_p, \vec{\pi}) \\ &\quad + \hat{s}_{i,j}^{shad-b,angular}(\vec{x}_p, \vec{\omega}_p, \vec{\pi}) \end{aligned} \quad (61)$$

where

$$\begin{aligned} \hat{s}_{i,j}^{shad-b,spatial}(\vec{x}_p, \vec{\omega}_p, \vec{\pi}) &= \\ &\quad \rho \frac{\vec{v}_{i,j} \cdot \vec{n}_i}{\vec{\omega}_p \cdot \vec{n}_i} (\vec{\omega}_s \times \vec{\omega}_p) \cdot \vec{t}_{i',k} I(\vec{x}_{p'}, \vec{\omega}_s, \vec{\pi}) \end{aligned} \quad (62)$$

and

$$\begin{aligned} \vec{s}_{i,j}^{shad-b,angular}(\vec{x}_p, \vec{\omega}_p, \vec{\pi}) = & \\ & - \rho l_{shad-b}(\vec{\omega}_s \times \vec{a} \times \vec{\omega}_s) \cdot \vec{t}_{i',k} I(\vec{x}_{p'}, \vec{\omega}_s, \vec{\pi}) \\ & + \rho l_{shad-b}(\vec{\omega}_s \times \vec{a}' \times \vec{\omega}_s) \cdot \vec{t}_{i',k} I(\vec{x}_{p'}, \vec{\omega}_s, \vec{\pi}). \end{aligned} \quad (63)$$

$\vec{t}_{i',k}$ are the vectors of circulation of $\mathcal{H}_{i'}^+$ [33], see Fig.19 and l_{shad-b} is the length of optical path between $\vec{x}_{p'}$ and \vec{x}_p (Fig.17).

The boundary condition of the rearward surface \mathcal{H}_i^- can be developed based on the general model of opaque-black surface in [33]:

$$s(\vec{x}_b, \vec{\omega}_s, \vec{\pi}) = \vec{s}_{i,j}^{shad-f}(\vec{x}_b, \vec{\omega}_s, \vec{\pi}) \quad (64)$$

and $\vec{s}_{i,j}^{shad-f}$ is the source on the border of the heliostat \mathcal{H}_i^- :

$$\begin{aligned} \vec{s}_{i,j}^{shad-f}(\vec{x}_b, \vec{\omega}_b, \vec{\pi}) = & \\ & (\vec{\omega}_s \times \vec{v}_{i,j}) \cdot \vec{t}_{i,k} I(\vec{x}_b, \vec{\omega}_s, \vec{\pi}) \end{aligned} \quad (65)$$

B Integral formulations

The vectors of contributions of \mathcal{S} defined in Section.3.2 are the sum of the vectors of sources captured by the receiver \mathcal{R} respectively. $\vec{S}_i^{tar,spatial}(\vec{\pi})$ is estimated by integrating $\vec{s}_i^{tar,spatial}$ on $\partial\mathcal{H}_i^+$ and on Ω_s :

$$\begin{aligned} \vec{S}_i^{tar,spatial}(\vec{\pi}) = & \oint_{\partial\mathcal{H}_i^+} d\vec{x}_p \int_{\Omega_s} d\vec{\omega}_s \\ & \left\{ \mathcal{H}(hit_f \in \mathcal{R}) \vec{s}_i^{tar,spatial}(\vec{x}_p, \vec{\omega}_p, \vec{\pi}) \right\} \end{aligned} \quad (66)$$

where the Heaviside function $\mathcal{H}(hit_f \in \mathcal{R})$ corresponds to a forward ray-tracing test which will be true if the source arrives at \mathcal{R} (the ray staring at \vec{x}_p , following $\vec{\omega}_p$ impacts the receiver \mathcal{R}).

$\vec{S}_i^{tar,angular}(\vec{\pi})$ is estimated by integrating $\vec{s}_i^{tar,angular}$ on \mathcal{H}_i^+ and on $\partial\Omega_s$:

$$\begin{aligned} \vec{S}_i^{tar,angular}(\vec{\pi}) = & \int_{\mathcal{H}_i^+} d\vec{x}_p \oint_{\partial\Omega_s} d\vec{\omega}_s \\ & \left\{ \mathcal{H}(hit_f \in \mathcal{R}) \vec{s}_i^{tar,angular}(\vec{x}_p, \vec{\omega}_p, \vec{\pi}) \right\} \end{aligned} \quad (67)$$

$\vec{S}_i^{blo}(\vec{\pi})$ is estimated by integrating \vec{s}_i^{blo} on $\partial\mathcal{H}_i^+$ and on Ω_s :

$$\begin{aligned} \vec{S}_i^{blo}(\vec{\pi}) = & \oint_{\partial\mathcal{H}_i^+} d\vec{x}_p \int_{\Omega_s} d\vec{\omega}_s \\ & \left\{ \mathcal{H}(hit_f \in \mathcal{R}) \vec{s}_i^{blo}(\vec{x}_p, \vec{\omega}_p, \vec{\pi}) \right\} \end{aligned} \quad (68)$$

$\vec{S}_i^{shad-b}(\vec{\pi})$ is estimated by integrating \vec{s}_i^{shad-b} on all the borders of other heliostats in the field $\partial\mathcal{H}_{i'}^+$ and on Ω_s :

$$\vec{S}_i^{shad-b}(\vec{\pi}) = \sum_{i'=1}^{n_{\mathcal{H}}, i' \neq i} \oint_{\partial\mathcal{H}_{i'}^+} d\vec{x}_p \int_{\Omega_s} d\vec{\omega}_s \left\{ \mathcal{H}(\text{hit}_f \in \mathcal{R}) \vec{s}_i^{shad-b}(\vec{x}_p, \vec{\omega}_p, \vec{\pi}) \right\} \quad (69)$$

$\vec{S}_i^{shad-f}(\vec{\pi})$ is estimated by integrating \vec{s}_i^{shad-f} on $\partial\mathcal{H}_i^-$ and on Ω_s :

$$\vec{S}_i^{shad-f}(\vec{\pi}) = \oint_{\partial\mathcal{H}_i^-} d\vec{x}_b \int_{\Omega_s} d\vec{\omega}_s \left\{ \mathcal{H}(\text{hit}_f \in \mathcal{R}) \vec{s}_i^{shad-f}(\vec{x}_b, \vec{\omega}_b, \vec{\pi}) \right\} \quad (70)$$

Finally, the corresponding integral formulations of $\vec{S}^{tar}(\vec{\pi})$, $\vec{S}^{tar}(\vec{\pi})$, $\vec{S}^{blo}(\vec{\pi})$, $\vec{S}^{shad-b}(\vec{\pi})$ and $\vec{S}^{shad-f}(\vec{\pi})$ are shown in Section.3.

C Explicit expression of Monte-Carlo weight

C.1 Contribution of targeting

We substitute Eq.56 into Eq.42, as well as Eq.57 into Eq.43. The following explicit expressions of Monte-Carlo weight are then yielded:

$$\vec{w}_1 = -l_k DNI \begin{bmatrix} (\vec{\omega}_p \times \vec{v}_{i,1}) \cdot \vec{t}_{i,k} \\ (\vec{\omega}_p \times \vec{v}_{i,2}) \cdot \vec{t}_{i,k} \\ (\vec{\omega}_p \times \vec{v}_{i,3}) \cdot \vec{t}_{i,k} \\ (\vec{\omega}_p \times \vec{v}_{i,4}) \cdot \vec{t}_{i,k} \\ (\vec{\omega}_p \times \vec{v}_{i,5}) \cdot \vec{t}_{i,k} \\ (\vec{\omega}_p \times \vec{v}_{i,6}) \cdot \vec{t}_{i,k} \end{bmatrix}; \quad (71)$$

$$\vec{w}_2 = 2\pi I_0 \mathcal{S}_{\mathcal{H}_i^+} |\vec{\omega}'_s \cdot \vec{n}_i| \begin{bmatrix} 0 \\ 0 \\ 0 \\ -2(\vec{\omega}'_s \times \vec{a}_{i,\theta}) \cdot \vec{\omega}_c \\ (\vec{\omega}'_s \times (\vec{a}'_{i,\phi} - \vec{a}_{i,\phi})) \cdot \vec{\omega}_c \\ 0 \end{bmatrix}. \quad (72)$$

where $\mathcal{S}_{\mathcal{H}_i^+}$ the area of the reflecting surface of the heliostat \mathcal{H}_i^+ , l_k the length of k^{th} side of the heliostat \mathcal{H}_i and $\vec{t}_{i,k}$ the vectors of circulation which is clockwise around the normal \vec{n}_i following the convention of [33], see Fig.19. $\vec{v}_{i,j}$ is the velocity of deformation linked to the point \vec{x}'_{p1} . Generally, it is a function of a point \vec{x} on the heliostat \mathcal{H}_i :

$$\vec{v}_{i,j} \equiv \vec{v}_{i,j}(\vec{x}). \quad (73)$$

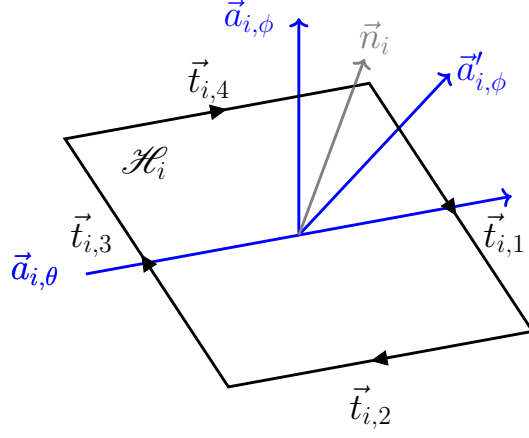


Figure 19: $\vec{t}_{i,k}$ are the clockwise vectors of circulation around \vec{n}_i

The vectors of $\vec{v}_{i,j}$ are given by Table.8, where $\vec{e} = \vec{x} - \vec{x}_{c,i}$ and $\vec{x}_{c,i}$ is the central position of the heliostat \mathcal{H}_i . The demonstrations are in Appendix.D and for example, the field of $\vec{v}_{i,4}(\vec{x}_p)$ and $\vec{v}_{i,5}(\vec{x}_p)$ are shown in Fig.20 and Fig.21.

| $\vec{v}_{i,1}$ | $\vec{v}_{i,2}$ | $\vec{v}_{i,3}$ | $\vec{v}_{i,4}$ | $\vec{v}_{i,5}$ | $\vec{v}_{i,6}$ |
|-----------------|-----------------|-----------------|-------------------------------------|-----------------------------------|-----------------------|
| $[1, 0, 0]$ | $[0, 1, 0]$ | $[0, 0, 1]$ | $\vec{a}_{i,\theta} \times \vec{e}$ | $\vec{a}_{i,\phi} \times \vec{e}$ | $\frac{\vec{e}}{l_k}$ |

Table 8: Components of $\vec{v}_{i,j}$ for a point \vec{x} on \mathcal{H}_i

In Eq.72, $\vec{a}_{i,\theta}$ is the axis of rotation related to $\vec{\pi}_{i,4}$ and $\vec{a}_{i,\phi}$ the axis of rotation related to $\vec{\pi}_{i,5}$. $\vec{a}'_{i,\phi}$ is the vector reflected by \mathcal{H}_i^+ from $-\vec{a}_{i,\phi}$ [33], see Fig.19.

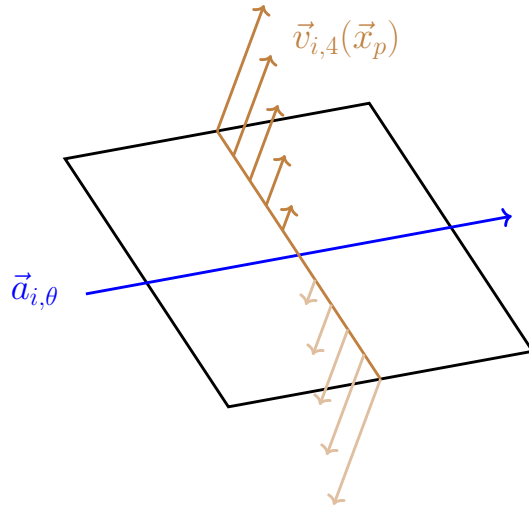


Figure 20: Schema of the field of $\vec{v}_{i,4}(\vec{x}_p)$

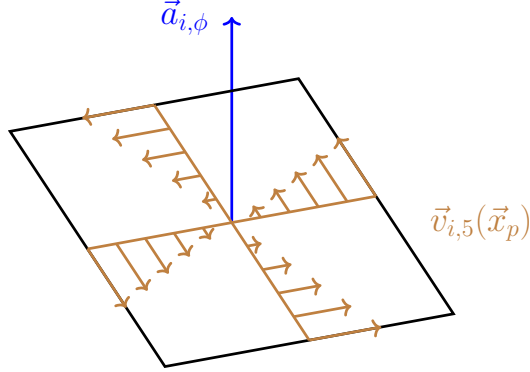


Figure 21: Schema of the field of $\vec{v}_{i,5}(\vec{x}_p)$

C.2 Contribution of backward-blocking

We substitute Eq.60 into Eq.45. The following explicit expression of Monte-Carlo weight is then yielded:

$$\vec{w}_3 = l_k DNI \begin{bmatrix} (\vec{\omega}_p \times \vec{v}_{i,1}) \cdot \vec{t}_{i,k} \\ (\vec{\omega}_p \times \vec{v}_{i,2}) \cdot \vec{t}_{i,k} \\ (\vec{\omega}_p \times \vec{v}_{i,3}) \cdot \vec{t}_{i,k} \\ (\vec{\omega}_p \times \vec{v}_{i,4}) \cdot \vec{t}_{i,k} \\ (\vec{\omega}_p \times \vec{v}_{i,5}) \cdot \vec{t}_{i,k} \\ (\vec{\omega}_p \times \vec{v}_{i,6}) \cdot \vec{t}_{i,k} \end{bmatrix}; \quad (74)$$

C.3 Contribution of forward-shadowing

We substitute Eq.65 into Eq.47. The following explicit expression of Monte-Carlo weight is then yielded:

$$\vec{w}_4 = -l_k DNI \begin{bmatrix} (\vec{\omega}_s \times \vec{v}_{i,1}) \cdot \vec{t}_{i,k} \\ (\vec{\omega}_s \times \vec{v}_{i,2}) \cdot \vec{t}_{i,k} \\ (\vec{\omega}_s \times \vec{v}_{i,3}) \cdot \vec{t}_{i,k} \\ (\vec{\omega}_s \times \vec{v}_{i,4}) \cdot \vec{t}_{i,k} \\ (\vec{\omega}_s \times \vec{v}_{i,5}) \cdot \vec{t}_{i,k} \\ (\vec{\omega}_s \times \vec{v}_{i,6}) \cdot \vec{t}_{i,k} \end{bmatrix}. \quad (75)$$

C.4 Contribution of backward-shadowing

We substitute Eq.62 into Eq.49, as well as Eq.63 into Eq.50. The following explicit expressions of Monte-Carlo weight are then yielded:

with

$$\vec{w}_5 = \rho l_k DNI \begin{bmatrix} \frac{\vec{v}_{i,1} \cdot \vec{n}_i}{\vec{\omega}_p \cdot \vec{n}_i} (\vec{\omega}_s \times \vec{\omega}_p) \cdot \vec{t}'_{i,k} \\ \frac{\vec{v}_{i,2} \cdot \vec{n}_i}{\vec{\omega}_p \cdot \vec{n}_i} (\vec{\omega}_s \times \vec{\omega}_p) \cdot \vec{t}'_{i,k} \\ \frac{\vec{v}_{i,3} \cdot \vec{n}_i}{\vec{\omega}_p \cdot \vec{n}_i} (\vec{\omega}_s \times \vec{\omega}_p) \cdot \vec{t}'_{i,k} \\ \frac{\vec{v}_{i,4} \cdot \vec{n}_i}{\vec{\omega}_p \cdot \vec{n}_i} (\vec{\omega}_s \times \vec{\omega}_p) \cdot \vec{t}'_{i,k} \\ \frac{\vec{v}_{i,5} \cdot \vec{n}_i}{\vec{\omega}_p \cdot \vec{n}_i} (\vec{\omega}_s \times \vec{\omega}_p) \cdot \vec{t}'_{i,k} \\ \frac{\vec{v}_{i,6} \cdot \vec{n}_i}{\vec{\omega}_p \cdot \vec{n}_i} (\vec{\omega}_s \times \vec{\omega}_p) \cdot \vec{t}'_{i,k} \end{bmatrix} \quad (76)$$

and

$$\vec{w}_6 = \rho l_k DNI l_{shad-b} \begin{bmatrix} 0 \\ 0 \\ 0 \\ -2(\vec{\omega}_s \times \vec{a}_{i,\theta} \times \vec{\omega}_s) \cdot \vec{t}'_{i,k} \\ (\vec{\omega}_s \times (\vec{a}_{i,\phi} - \vec{a}_{i,\phi'}) \times \vec{\omega}_s) \cdot \vec{t}'_{i,k} \\ 0 \end{bmatrix} \quad (77)$$

D Velocity of deformation

Following [33], we need to define a geometric space, and a material space for a heliostat \mathcal{H}_i , and special notations are needed to calculate the velocity of deformation. In geometric space, the positions \vec{y} and directions $\vec{\omega}$ are functions of the geometric parameter $\vec{\pi}_{i,j}$, while in material space, the positions are noted \vec{y} and directions are noted $\vec{\omega}$. They are not depended on $\vec{\pi}_{i,j}$.

The function Z and Ω link the two spaces so that the positions and directions in one space can refer to the other space:

$$\vec{y} = Z(\vec{y}, \vec{\pi}_{i,j}); \vec{\omega} = \Omega(\vec{\omega}, \vec{\pi}) \quad (78)$$

We define the velocity of deformation $\vec{v}_{i,j}$ as the derivative of Z with respect to $\vec{\pi}_{i,j}$:

$$\vec{v}_{i,j} \equiv \partial_{\vec{\pi}_{i,j}} Z(\vec{y}, \vec{\pi}_{i,j}) \quad (79)$$

For different $\vec{\pi}_{i,j}$, the velocities of deformations $\vec{v}_{i,j}$ are summarized in Table.9, where \vec{a}_θ and \vec{a}_ϕ are two axes of rotation for the heliostat \mathcal{H}_i (in Fig.4) and l_k the original length of size of the heliostat.

| | $Z(\vec{y}, \tilde{\pi}_{i,j})$ | $\vec{v} = \partial_{\tilde{\pi}} Z$ |
|---------------------|---|---|
| $\tilde{\pi}_{i,1}$ | $\begin{bmatrix} \tilde{\pi}_{i,1} \\ 0 \\ 0 \end{bmatrix} + \vec{y}$ | $\vec{v} = \begin{bmatrix} 1 \\ 0 \\ 0 \end{bmatrix}$ |
| $\tilde{\pi}_{i,2}$ | $\begin{bmatrix} 0 \\ \tilde{\pi}_{i,2} \\ 0 \end{bmatrix} + \vec{y}$ | $\vec{v} = \begin{bmatrix} 0 \\ 1 \\ 0 \end{bmatrix}$ |
| $\tilde{\pi}_{i,3}$ | $\begin{bmatrix} 0 \\ 0 \\ \tilde{\pi}_{i,3} \end{bmatrix} + \vec{y}$ | $\vec{v} = \begin{bmatrix} 0 \\ 0 \\ 1 \end{bmatrix}$ |
| $\tilde{\pi}_{i,4}$ | $\vec{y} + \tilde{\pi}_{i,4}(\vec{a}_{i,\theta} \times \vec{y})$ | $\vec{a}_{i,\theta} \times \vec{y}$ |
| $\tilde{\pi}_{i,5}$ | $\vec{y} + \tilde{\pi}_{i,5}(\vec{a}_{i,\phi} \times \vec{y})$ | $\vec{a}_{i,\phi} \times \vec{y}$ |
| $\tilde{\pi}_{i,6}$ | $\frac{\tilde{\pi}_{i,6}}{l_k} \vec{y}$ | $\frac{\vec{y}}{l_k}$ |

Table 9: The functions Z and \vec{v} for the 6 geometric parameters of heliostat

E Algorithms

Algorithm 2 Estimate P

Input: Geometry of heliostats and receiver, $\vec{\omega}_c, N$

▷ N number of realizations

Initialization: $n \leftarrow 0, sum \leftarrow 0, sum2 \leftarrow 0$

while $n < N$ **do**

 Sample \vec{x}_{p1} on $\mathcal{S}_{\mathcal{H}^+}$ based on p_X

 Sample $\vec{\omega}_s$ within Ω_s based on p_{Ω_s} .

 Compute $\vec{\omega}_p$ by the law of specular reflection

 Get \vec{x}_{p0} from \vec{x}_{p1} following $-\vec{\omega}_s$

 Get \vec{x}_{p2} from \vec{x}_{p1} following $\vec{\omega}_p$

if $\vec{x}_{p0} \in \mathcal{O}_s$ & $\vec{x}_{p2} \in \mathcal{R}$ **then**

 Compute \hat{w}

$sum \leftarrow sum + \hat{w}$

$sum2 \leftarrow sum2 + \hat{w}^2$

else

$sum \leftarrow sum + 0$

$sum2 \leftarrow sum2 + 0$

end if

$n \leftarrow n + 1$

end while

Output: $P \leftarrow \frac{sum}{N}, \sigma(P) \leftarrow \sqrt{\frac{sum2 - (\frac{sum}{N})^2}{N-1}}$

Algorithm 3 Estimate \vec{S}_i^{tar} and $\vec{\sigma}(\vec{S}_i^{tar})$

Input: Geometry of heliostats and receiver, $\vec{\omega}_c$, N
 $\triangleright N$ number of realizations

Initialization: $\vec{S}_i^{tar} \leftarrow \mathbf{0}$, $\vec{\sigma}(\vec{S}_i^{tar}) \leftarrow \mathbf{0}$
while $k < 4$ **do**
 $\triangleright \mathcal{H}_i$ has 4 borders

Initialization: $n \leftarrow 0$, $\overrightarrow{sum} \leftarrow \mathbf{0}$, $\overrightarrow{sum2} \leftarrow \mathbf{0}$
while $n < N$ **do**

Sample \vec{x}'_{p1} on l_k based on p_X

Sample $\vec{\omega}'_s$ within Ω_s based on p_{Ω_s} .

Compute $\vec{\omega}'_p$ based on $\vec{\omega}'_s$ and \vec{n}_i by the law of specular reflection

Get \vec{x}'_{p0} from \vec{x}'_{p1} following $-\vec{\omega}'_s$

Get \vec{x}'_{p2} from \vec{x}'_{p1} following $\vec{\omega}'_p$
if $\vec{x}'_{p0} \in \mathcal{O}_s$ & $\vec{x}'_{p2} \in \mathcal{R}$ **then**

Compute \vec{w}_1
 $\overrightarrow{sum} \leftarrow \overrightarrow{sum} + \vec{w}_1$
 $\overrightarrow{sum2} \leftarrow \overrightarrow{sum2} + \vec{w}_1^2$
else
 $\overrightarrow{sum} \leftarrow \overrightarrow{sum} + \mathbf{0}$
 $\overrightarrow{sum2} \leftarrow \overrightarrow{sum2} + \mathbf{0}$
end if
 $n \leftarrow n + 1$
end while
 $\vec{S}_i^{tar} \leftarrow \vec{S}_i^{tar} + \frac{\overrightarrow{sum}}{N}$, $\vec{\sigma}(\vec{S}_i^{tar}) \leftarrow \vec{\sigma}(\vec{S}_i^{tar}) + \sigma(P) \leftarrow \sqrt{\frac{\overrightarrow{sum2} - (\frac{\overrightarrow{sum}}{N})^2}{N-1}}$
 $k \leftarrow k + 1$
end while

Initialization: $n \leftarrow 0$, $\overrightarrow{sum} \leftarrow \mathbf{0}$, $\overrightarrow{sum2} \leftarrow \mathbf{0}$
while $n < N$ **do**
 $\triangleright N$ number of realizations

Sample \vec{x}_{p1} on $\mathcal{S}_{\mathcal{H}_i^+}$ based on p_{X_i}

Sample $\vec{\omega}'_s$ on $\partial\Omega_s$ based on $p_{\Omega'_s}$.

Compute $\vec{\omega}'_p$ based on $\vec{\omega}'_s$ and \vec{n}_i by the law of specular reflection

Get \vec{x}_{p0} from \vec{x}_{p1} following $-\vec{\omega}'_s$

Get \vec{x}_{p2} from \vec{x}_{p1} following $\vec{\omega}'_p$
if $\vec{x}_{p0} \in \mathcal{O}_s$ & $\vec{x}_{p2} \in \mathcal{R}$ **then**

Compute \vec{w}_2
 $\overrightarrow{sum} \leftarrow \overrightarrow{sum} + \vec{w}_2$
 $\overrightarrow{sum2} \leftarrow \overrightarrow{sum2} + \vec{w}_2^2$
else
 $\overrightarrow{sum} \leftarrow \overrightarrow{sum} + \mathbf{0}$
 $\overrightarrow{sum2} \leftarrow \overrightarrow{sum2} + \mathbf{0}$
end if
 $n \leftarrow n + 1$
end while
 $\vec{S}_i^{tar} \leftarrow \vec{S}_i^{tar} + \frac{\overrightarrow{sum}}{N}$, $\vec{\sigma}(\vec{S}_i^{tar}) \leftarrow \vec{\sigma}(\vec{S}_i^{tar}) + \sigma(P) \leftarrow \sqrt{\frac{\overrightarrow{sum2} - (\frac{\overrightarrow{sum}}{N})^2}{N-1}}$
Output: \vec{S}_i^{tar} , $\vec{\sigma}(\vec{S}_i^{tar})$

Algorithm 4 Estimate \vec{S}_i^{blo} and $\vec{\sigma}(\vec{S}_i^{blo})$

Input: Geometry of heliostats and receiver, $\vec{\omega}_c, N, i$ ▷ N number of realizations

Initialization: $i' \leftarrow 0, \vec{S}_i^{blo} \leftarrow \mathbf{0}, \vec{\sigma}(\vec{S}_i^{blo}) \leftarrow \mathbf{0}$ ▷ i' index of heliostat being blocked

while $i' < n_{\mathcal{H}}$ **do** ▷ $n_{\mathcal{H}}$ number of heliostats

Compute the distance $l_{i,i'}$ between \mathcal{H}_i and $\mathcal{H}_{i'}$

if $l_{i,i'} < l_d$ & $i' \neq i$ **then**

▷ Ignore the too-far-away heliostats for backward-blocking effect

Initialization: $k \leftarrow 0$

while $k < 4$ **do** ▷ \mathcal{H}_i has 4 borders

Initialization: $n \leftarrow 0, \vec{sum} \leftarrow \mathbf{0}, \vec{sum2} \leftarrow \mathbf{0}$

while $n < N$ **do**

Sample \vec{x}'_{p2} on l_k based on $p_{X'}$

Sample $\vec{\omega}_s$ within Ω_s based on p_{Ω_s} .

Compute $\vec{\omega}_p$ based on $\vec{\omega}_s$ and $\vec{n}_{i'}$ by the law of specular reflection

Get \vec{x}'_{p1} from \vec{x}'_{p2} following $-\vec{\omega}_p$

Get \vec{x}'_{p0} from \vec{x}'_{p1} following $-\vec{\omega}_s$

Get \vec{x}'_{p3} from \vec{x}'_{p2} following $\vec{\omega}_p$

if $\vec{x}'_{p0} \in \mathcal{O}_s$ & $\vec{x}'_{p1} \in \mathcal{H}_{i'}^+$ & $\vec{x}'_{p3} \in \mathcal{R}$ **then**

Compute \vec{w}

$\vec{sum} \leftarrow \vec{sum} - \vec{w}_1$

$\vec{sum2} \leftarrow \vec{sum2} - \vec{w}_1^2$

else

$\vec{sum} \leftarrow \vec{sum} + \mathbf{0}$

$\vec{sum2} \leftarrow \vec{sum2} + \mathbf{0}$

end if

$n \leftarrow n + 1$

end while

$k \leftarrow k + 1$

$\vec{S}_i^{blo} \leftarrow \vec{S}_i^{blo} + \frac{\vec{sum}}{N}, \vec{\sigma}(\vec{S}_i^{blo}) \leftarrow \vec{\sigma}(\vec{S}_i^{blo}) + \sigma(P) \leftarrow \sqrt{\frac{\vec{sum2} - (\frac{\vec{sum}}{N})^2}{N-1}}$

end while

end if

$i' \leftarrow i' + 1$

end while

Output: $\vec{S}_i^{blo}, \vec{\sigma}(\vec{S}_i^{blo})$

Algorithm 5 Estimate \vec{S}_i^{shad-f} and $\vec{\sigma}(\vec{S}_i^{shad-f})$

Input: Geometry of heliostats and receiver, $\vec{\omega}_c, N$

$\triangleright N$ number of realizations

Initialization: $k \leftarrow 0, \vec{S}_i^{shad-f} \leftarrow \mathbf{0}, \vec{\sigma}(\vec{S}_i^{shad-f}) \leftarrow \mathbf{0}$

while $k < 4$ **do** $\triangleright \mathcal{H}_i$ has 4 borders

Initialization: $n \leftarrow 0, \overrightarrow{sum} \leftarrow \mathbf{0}, \overrightarrow{sum2} \leftarrow \mathbf{0}$

while $n < N$ **do**

Sample \vec{x}'_{p1} on l_k of \mathcal{H}_i^+ based on $p_{X'}$

Sample $\vec{\omega}_s$ within Ω_s based on p_{Ω_s} .

Get \vec{x}'_{p2} from \vec{x}'_{p1} following $\vec{\omega}_s$

Get the normal $\vec{n}_{i'}$ on \vec{x}'_{p2}

Compute $\vec{\omega}_p$ based on $\vec{\omega}_s$ and $\vec{n}_{i'}$ by the law of specular reflection

Get \vec{x}'_{p0} from \vec{x}'_{p1} following $-\vec{\omega}_s$

Get \vec{x}'_{p3} from \vec{x}'_{p2} following $\vec{\omega}_p$

if $\vec{x}'_{p0} \in \mathcal{O}_s$ & $\vec{x}'_{p1} \in \mathcal{H}^+$ & $\vec{x}'_{p3} \in \mathcal{R}$ **then**

Compute \vec{w}

$\overrightarrow{sum} \leftarrow \overrightarrow{sum} + \vec{w}_3$

$\overrightarrow{sum2} \leftarrow \overrightarrow{sum2} + \vec{w}_3^2$

else

$\overrightarrow{sum} \leftarrow \overrightarrow{sum} + \mathbf{0}$

$\overrightarrow{sum2} \leftarrow \overrightarrow{sum2} + \mathbf{0}$

end if

$n \leftarrow n + 1$

end while

$k \leftarrow k + 1$

end while

$\vec{S}_i^{shad-f} \leftarrow \vec{S}_i^{shad-f} + \frac{\overrightarrow{sum}}{N}, \vec{\sigma}(\vec{S}_i^{shad-f}) \leftarrow \vec{\sigma}(\vec{S}_i^{shad-f}) + \sigma(P) \leftarrow$

$\sqrt{\frac{\overrightarrow{sum2} - (\frac{\overrightarrow{sum}}{N})^2}{N-1}}$

Output: $\vec{S}_i^{shad-f}, \vec{\sigma}(\vec{S}_i^{shad-f})$

Algorithm 6 Estimate \vec{S}_i^{shad-b} and $\vec{\sigma}(\vec{S}_i^{shad-b})$

Input: Geometry of heliostats and receiver, $\vec{\omega}_c, N, i$
 $\triangleright N$ number of realizations

Initialization: $i' \leftarrow 0, \vec{S}_i^{shad-b} \leftarrow \mathbf{0}, \vec{\sigma}(\vec{S}_i^{shad-b}) \leftarrow \mathbf{0}$ $\triangleright i'$ index of shadowing heliostat

while $i' < n_{\mathcal{H}}$ **do** $\triangleright n_{\mathcal{H}}$ number of heliostats

 Compute the distance $l_{i,i'}$ between \mathcal{H}_i and $\mathcal{H}_{i'}$

if $l_{i,i'} < l_d$ & $i' \neq i$ **then**

\triangleright Ignore the too-far-away heliostats for backward-shadowing effect

 Initialization: $k \leftarrow 0$

while $k < 4$ **do** \triangleright loop all borders on $\mathcal{H}_{i'}$

 Initialization: $n \leftarrow 0, \overrightarrow{sum\hat{m}} \leftarrow \mathbf{0}, \overrightarrow{sum\hat{z}} \leftarrow \mathbf{0}$

while $n < N$ **do**

 Sample \vec{x}'_{p1} on l_k of $\mathcal{H}_{i'}$ based on p_X .

 Sample $\vec{\omega}_s$ within Ω_s based on p_{Ω_s} .

 Get \vec{x}'_{p2} from \vec{x}'_{p1} following $\vec{\omega}_s$

 Compute $\vec{\omega}_p$ based on $\vec{\omega}_s$ and \vec{n}_i by the law of specular reflection

 Get \vec{x}'_{p0} from \vec{x}'_{p1} following $-\vec{\omega}_s$

 Get \vec{x}'_{p3} from \vec{x}'_{p2} following $\vec{\omega}_p$

if $\vec{x}'_{p0} \in \mathcal{O}_s$ & $\vec{x}'_{p2} \in \mathcal{H}_i^+$ & $\vec{x}'_{p3} \in \mathcal{R}$ **then**

 Compute \vec{w}_4 and \vec{w}_5

$\overrightarrow{sum\hat{m}} \leftarrow \overrightarrow{sum\hat{m}} + \vec{w}_4 + \vec{w}_5$

$\overrightarrow{sum\hat{z}} \leftarrow \overrightarrow{sum\hat{z}} + (\vec{w}_4 + \vec{w}_5)^2$

else

$\overrightarrow{sum\hat{m}} \leftarrow \overrightarrow{sum\hat{m}} + \mathbf{0}$

$\overrightarrow{sum\hat{z}} \leftarrow \overrightarrow{sum\hat{z}} + \mathbf{0}$

end if

$n \leftarrow n + 1$

end while

$k \leftarrow k + 1$

$\vec{S}_i^{shad-b} \leftarrow \vec{S}_i^{shad-b} + \frac{\overrightarrow{sum\hat{m}}}{N}, \vec{\sigma}(\vec{S}_i^{shad-b}) \leftarrow \vec{\sigma}(\vec{S}_i^{shad-b}) + \sigma(P) \leftarrow$

$\sqrt{\frac{\overrightarrow{sum\hat{z}} - (\frac{\overrightarrow{sum\hat{m}}}{N})^2}{N-1}}$

end while

end if

$i' \leftarrow i' + 1$

end while

Output: $\vec{S}_i^{shad-b}, \vec{\sigma}(\vec{S}_i^{shad-b})$

References

- [1] Clifford K Ho. Advances in central receivers for concentrating solar applications. *Solar energy*, 152:38–56, 2017.
- [2] Reiner Buck. Heliostat field layout improvement by nonrestricted refinement. *Journal of solar energy engineering*, 136(2), 2014.
- [3] Lorin L Vant-Hull. An educated ray trace approach to solar tower optics. *Optical Engineering*, 16(5):497–504, 1977.
- [4] FW Lipps and Lorin L Vant-Hull. User manual for the university of houston solar central receiver, cellwise performance model: Ns. Technical report, Houston Univ., TX (USA). Energy Lab., 1980.
- [5] Lifeng Li, Joe Coventry, Roman Bader, John Pye, and Wojciech Lipiński. Optics of solar central receiver systems: a review. *Optics express*, 24(14):A985–A1007, 2016.
- [6] Manuel J Blanco, Amaia Mutuberría, Pierre Garcia, Raquel Gastesi, and Victor Martin. Preliminary validation of tonatiuh. In *SolarPACES conference*, 2009.
- [7] Cyril Caliot, Hadrien Benoit, Emmanuel Guillot, Jean-Louis Sans, Alain Ferriere, Gilles Flamant, Christophe Coustet, and Benjamin Piaud. Validation of a monte carlo integral formulation applied to solar facility simulations and use of sensitivities. *Journal of Solar Energy Engineering*, 137(2):021019, 2015.
- [8] PL Leary and JD Hankins. User’s guide for mirval: a computer code for comparing designs of heliostat-receiver optics for central receiver solar power plants. Technical report, Sandia National Lab.(SNL-CA), Livermore, CA (United States), 1979.
- [9] Tim Wendelin. Soltrace: a new optical modeling tool for concentrating solar optics. In *International solar energy conference*, volume 36762, pages 253–260, 2003.
- [10] Peter Schwarzbözl, Robert Pitz-Paal, and Mark Schmitz. Visual hflcal-a software tool for layout and optimisation of heliostat fields. In *Proceedings*, 2009.
- [11] Charles N Vittitoe and Frank Biggs. User’s guide to helios: a computer program for modeling the optical behavior of reflecting solar concentrators. part iii. appendices concerning helios-code details. Technical report, Sandia National Lab.(SNL-NM), Albuquerque, NM (United States), 1981.
- [12] Michael J Wagner and Tim Wendelin. Solarpilot: A power tower solar field layout and characterization tool. *Solar Energy*, 171:185–196, 2018.
- [13] Pierre Garcia, Alain Ferriere, and Jean-Jacques Beziau. Codes for solar flux calculation dedicated to central receiver system applications: A comparative review. *Solar Energy*, 82(3):189–197, 2008.

- [14] Ye Wang, Daniel Potter, Charles-Alexis Asselineau, Clotilde Corsi, Michael Wagner, Cyril Caliot, Benjamin Piaud, Manuel Blanco, Jin-Soo Kim, and John Pye. Verification of optical modelling of sunshape and surface slope error for concentrating solar power systems. *Solar Energy*, 195:461–474, 2020.
- [15] Robert Pitz-Paal, Nicolas Bayer Botero, and Aldo Steinfeld. Heliostat field layout optimization for high-temperature solar thermochemical processing. *Solar energy*, 85(2):334–343, 2011.
- [16] Olivier Farges, Jean-Jacques Bézian, Hélène Bru, Mouna El Hafi, Richard Fournier, and Christophe Spiesser. Life-time integration using monte carlo methods when optimizing the design of concentrated solar power plants. *Solar Energy*, 113:57–62, 2015.
- [17] Miguel Diago, Nicolas Calvet, and Peter R Armstrong. Net power maximization from a faceted beam-down solar concentrator. *Solar Energy*, 204:476–488, 2020.
- [18] Yiyi Zhou and Yuhong Zhao. Heliostat field layout design for solar tower power plant based on gpu. *IFAC Proceedings Volumes*, 47(3):4953–4958, 2014.
- [19] Y Favennec, F Dubot, D Le Hardy, B Rousseau, and DR Rousse. Space-dependent sobolev gradients as a regularization for inverse radiative transfer problems. *Mathematical Problems in Engineering*, 2016, 2016.
- [20] Seonghyeok Yang, Kyungeun Lee, and Ikjin Lee. Pattern-free heliostat field layout optimization using physics-based gradient. *Solar Energy*, 206:722–731, August 2020.
- [21] AJ Marston, KJ Daun, and MR Collins. Geometric optimization of concentrating solar collectors using monte carlo simulation. *Journal of solar energy engineering*, 132(4), 2010.
- [22] Andrew James Marston. Geometric optimization of solar concentrating collectors using quasi-monte carlo simulation. Master’s thesis, University of Waterloo, 2010.
- [23] Emmanuel Gobet. Stochastic differential equations and Feynman-Kac formulas. In *Monte-Carlo Methods and Stochastic Processes*. Chapman and Hall/CRC, 2016. Num Pages: 46.
- [24] Jérémie Delatorre, Germain Baud, Jean-Jacques Bézian, Stéphane Blanco, Cyril Caliot, Jean-François Cornet, Christophe Coustet, Jérémie Dauchet, Mouna El Hafi, Vincent Eymet, et al. Monte carlo advances and concentrated solar applications. *Solar Energy*, 103:653–681, 2014.
- [25] A De Lataillade, Stéphane Blanco, Y Clergent, Jean-Louis Dufresne, Mouna El Hafi, and Richard Fournier. Monte carlo method and sensitivity estimations. *Journal of Quantitative Spectroscopy and Radiative Transfer*, 75(5):529–538, 2002.

- [26] Maxime Roger, Stéphane Blanco, Mouna El Hafi, and Richard Fournier. Monte carlo estimates of domain-deformation sensitivities. *Physical review letters*, 95(18):180601, 2005.
- [27] P Lapeyre, Stéphane Blanco, Cyril Caliot, J Dauchet, Mouna El Hafi, Richard Fournier, Olivier Farges, Jacques Gautrais, and Maxime Roger. Monte-carlo and sensitivity transport models for domain deformation. *Journal of Quantitative Spectroscopy and Radiative Transfer*, 251:107022, 2020.
- [28] Cheng Zhang, Bailey Miller, Kan Yan, Ioannis Gkioulekas, and Shuang Zhao. Path-space differentiable rendering. *ACM transactions on graphics*, 39(4), 2020.
- [29] Cheng Zhang, Lifan Wu, Changxi Zheng, Ioannis Gkioulekas, Ravi Ramamoorthi, and Shuang Zhao. A differential theory of radiative transfer. *ACM Transactions on Graphics (TOG)*, 38(6):1–16, 2019.
- [30] Tzu-Mao Li, Miika Aittala, Frédo Durand, and Jaakko Lehtinen. Differentiable monte carlo ray tracing through edge sampling. *ACM Transactions on Graphics (TOG)*, 37(6):1–11, 2018.
- [31] Tizian Zeltner, Sébastien Speierer, Iliyan Georgiev, and Wenzel Jakob. Monte carlo estimators for differential light transport. *ACM Transactions on Graphics (TOG)*, 40(4):1–16, 2021.
- [32] Hiroharu Kato, Deniz Beker, Mihai Morariu, Takahiro Ando, Toru Matsuoka, Wadim Kehl, and Adrien Gaidon. Differentiable rendering: A survey. *arXiv preprint arXiv:2006.12057*, 2020.
- [33] Paule Lapeyre, Zili He, Stéphane Blanco, Cyril Caliot, Christophe Coustet, Jérémi Dauchet, Mouna El Hafi, Simon Eibner, Eugene d’Eon, Olivier Farges, Richard Fournier, Jacques Gautrais, Nada Chems Mourtaday, and Maxime Roger. A physical model and a monte carlo estimate for the specific intensity spatial derivative, angular derivative and geometric sensitivity, 2022.
- [34] Steve Schell. Design and evaluation of esolar’s heliostat fields. *Solar Energy*, 85(4):614–619, 2011.
- [35] Philippe Blanc, Bella Espinar, Norbert Geuder, Christian Gueymard, Richard Meyer, Robert Pitz-Paal, Bernhard Reinhardt, David Renné, Manajit Sengupta, Lucien Wald, et al. Direct normal irradiance related definitions and applications: The circumsolar issue. *Solar Energy*, 110:561–577, 2014.
- [36] John R Howell, M Pinar Mengüç, Kyle Daun, and Robert Siegel. *Thermal radiation heat transfer*. CRC press, 2020.
- [37] Daniel Buie, AG Monger, and CJ Dey. Sunshape distributions for terrestrial solar simulations. *Solar energy*, 74(2):113–122, 2003.
- [38] Charles N Vittitoe and Frank Biggs. Six-gaussian representation of the angular-brightness distribution for solar radiation. *Solar Energy*, 27(6):469–490, 1981.

- [39] Benjamin Piaud, Christophe Coustet, Cyril Caliot, Emmanuel Guillot, and Gilles Flamant. Application of Monte-Carlo sensitivities estimation in Solfast-4D. In *SolarPaces 2012 Conference*, pages 1–9, 2012.
- [40] William L Dunn and J Kenneth Shultis. *Exploring monte carlo methods*. Elsevier, 2011.